



# Examination of Relationship Between Photonic Signatures and Fracture Strength of Fused Silica Used in Orbiter Windows

*William T. Yost and K. Elliott Cramer  
Langley Research Center, Hampton, Virginia*

*Linda R. Estes  
Johnson Space Center, Houston, Texas*

*Jonathan A. Salem  
Glenn Research Center, Cleveland, Ohio*

*James Lankford, Jr.  
Southwest Research Institute, San Antonio, Texas*

*Jon Lesniak  
Stress Photonics, Inc., Madison, Wisconsin*

## NASA STI Program . . . in Profile

Since its founding, NASA has been dedicated to the advancement of aeronautics and space science. The NASA scientific and technical information (STI) program plays a key part in helping NASA maintain this important role.

The NASA STI program operates under the auspices of the Agency Chief Information Officer. It collects, organizes, provides for archiving, and disseminates NASA's STI. The NASA STI program provides access to the NASA Aeronautics and Space Database and its public interface, the NASA Technical Report Server, thus providing one of the largest collections of aeronautical and space science STI in the world. Results are published in both non-NASA channels and by NASA in the NASA STI Report Series, which includes the following report types:

- **TECHNICAL PUBLICATION.** Reports of completed research or a major significant phase of research that present the results of NASA programs and include extensive data or theoretical analysis. Includes compilations of significant scientific and technical data and information deemed to be of continuing reference value. NASA counterpart of peer-reviewed formal professional papers, but having less stringent limitations on manuscript length and extent of graphic presentations.
- **TECHNICAL MEMORANDUM.** Scientific and technical findings that are preliminary or of specialized interest, e.g., quick release reports, working papers, and bibliographies that contain minimal annotation. Does not contain extensive analysis.
- **CONTRACTOR REPORT.** Scientific and technical findings by NASA-sponsored contractors and grantees.
- **CONFERENCE PUBLICATION.** Collected papers from scientific and technical conferences, symposia, seminars, or other meetings sponsored or co-sponsored by NASA.
- **SPECIAL PUBLICATION.** Scientific, technical, or historical information from NASA programs, projects, and missions, often concerned with subjects having substantial public interest.
- **TECHNICAL TRANSLATION.** English-language translations of foreign scientific and technical material pertinent to NASA's mission.

Specialized services also include creating custom thesauri, building customized databases, and organizing and publishing research results.

For more information about the NASA STI program, see the following:

- Access the NASA STI program home page at <http://www.sti.nasa.gov>
- E-mail your question via the Internet to [help@sti.nasa.gov](mailto:help@sti.nasa.gov)
- Fax your question to the NASA STI Help Desk at 443-757-5803
- Phone the NASA STI Help Desk at 443-757-5802
- Write to:  
NASA STI Help Desk  
NASA Center for AeroSpace Information  
7115 Standard Drive  
Hanover, MD 21076-1320

NASA/TP-2011-217322



# Examination of Relationship Between Photonic Signatures and Fracture Strength of Fused Silica Used in Orbiter Windows

*William T. Yost and K. Elliott Cramer  
Langley Research Center, Hampton, Virginia*

*Linda R. Estes  
Johnson Space Center, Houston, Texas*

*Jonathan A. Salem  
Glenn Research Center, Cleveland, Ohio*

*James Lankford, Jr.  
Southwest Research Institute, San Antonio, Texas*

*Jon Lesniak  
Stress Photonics, Inc., Madison, Wisconsin*

National Aeronautics and  
Space Administration

Langley Research Center  
Hampton, Virginia 23681-2199

December 2011

The use of trademarks or names of manufacturers in this report is for accurate reporting and does not constitute an official endorsement, either expressed or implied, of such products or manufacturers by the National Aeronautics and Space Administration.

Available from:

NASA Center for AeroSpace Information  
7115 Standard Drive  
Hanover, MD 21076-1320  
443-757-5802

# Examination of Relationship between Photonic Signatures and Fracture Strength of Fused Silica Used in Orbiter Windows

William T. Yost and K. Elliott Cramer, NASA-Langley Research Center  
Lynda R. Estes, NASA-Johnson Space Center  
Jonathan A. Salem, NASA-Glenn Research Center  
James Lankford, Jr.-Southwest Research Institute  
and  
Jon Lesniak-Stress Photonics, Inc.

## Abstract

A commercially available grey-field polariscope (GFP) instrument for photoelastic examination is used to assess impact damage inflicted upon the outer-most pane of the orbiter windows. Four categories of damage: hyper-velocity impacts that occur during space-flight (HVI); hypervelocity impacts artificially made at the Hypervelocity Impact Technology Facility (HIT-F); impacts made by larger objects falling onto the pane surface to simulate dropped items on the window during service/storage of vehicle (Bruises); and light scratches from dull objects designed to mimic those that might occur by dragging a dull object across the glass surface (Chatter Checks) are examined. The damage sites are cored from fused silica window carcasses, examined with the GFP and other methodologies, and broken using the ASTM Standard C1499-09 to measure the fracture strength. A correlation is made between the fracture strength and damage-site measurements including geometrical measurements and GFP measurements of photoelastic retardation (stress patterns) surrounding the damage sites. An analytical damage model to predict fracture strength from photoelastic retardation measurements is presented and compared with experimental results, where a power-law correlation between the measurements and fracture strengths,  $\sigma_f$ , is shown to give the best fit. The best-fit results are found to be:

$$\sigma_f = 43.7 (\epsilon)^{-0.127} \quad R^2 = 0.997 \quad (\text{HVI-photoelastic retardation})$$

$$\sigma_f = 181 (\epsilon)^{-0.351} \quad R^2 = 0.955 \quad (\text{HIT-F-GFP measured inner diameter damage})$$

$$\sigma_f = 37.2 (\epsilon)^{-0.282} \quad R^2 = 0.981 \quad (\text{Bruises-photoelastic retardation})$$

$$\sigma_f = 117 (\epsilon)^{-0.099} \quad R^2 = 0.334 \quad (\text{Chatter Checks-outer length of scratch})$$

where  $\epsilon$  is the corresponding damage parameter (e.g. photoelastic retardation) measurement. Based on the analytical damage model a general experimental procedure outline is presented. The GFP is shown to be a viable instrument for use in the estimation of damage effects on the mechanical integrity of the outer-most window for manned space vehicles

## I. INTRODUCTION

During storage and flight, windows on space vehicles are subjected to sometimes harsh and damaging conditions capable of impairing their mechanical performance. The outer windowpanes on a spacecraft encounter high velocity impacts (HVI) from debris and micrometeoroids from vehicle launch to landing. During vehicle re-entry these windowpanes are subjected to high temperatures. While in storage and during preparation for launch, windows sometimes encounter accidental collision events, such as a dropped tool or a tethered device striking its surface.

Fused silica, which is the primary material of choice for crewed spacecraft windows for the manned spacecraft programs at NASA<sup>1</sup>, has significant advantages over other transparent materials. These include thermal shock tolerance and optical performance. With these advantages, however, are properties that make engineering with this material very difficult. Fused silica, like other silica-based glasses, is a brittle material, whose strength can be degraded considerably by sharp object impacts<sup>2,3</sup>. Other characteristics of engineering significance include a large scatter in material and fracture properties. In particular, fracture strength exhibits a strong dependence on surface quality (e.g. presence of micro-cracks and other flaws) and the inevitable internal flaws that are distributed through the volume.

From launch to landing the windowpanes on a spacecraft are subjected to aggressive conditions and events that degrade mechanical performance and affect vehicle safety. The vehicle's re-entry into the atmosphere subjects these windowpanes to high temperatures<sup>4</sup>. As a consequence of the temperature ranges encountered, the mounts must place the glass panes under minimum mechanical stresses (sufficient to seal the glass to the vehicle). When damaged by impacts and placed under tensile stresses, these panes can suddenly fail. All accumulated damage sites, whether from the active (launch to landing) period or from storage and maintenance period, must be identified, measured, evaluated, and continually monitored for their effects on the pane's structural performance. Since the service life of a pane is shortened by damage causing events, engineers must ensure that the glass surfaces are carefully inspected prior to every active cycle for safety assurance.

To date, the U.S Space Program has never lost a spacecraft to window failure. This is due in large part to a carefully designed program and execution of window maintenance procedures. During each mission, thousands of new damage sites are added to each pane. A crew dedicated to window maintenance conducted thorough post flight examinations of the Shuttle windows. The examination procedure used various and sometimes specially designed optical instruments. During the inspection the emphasis was placed on accurate measurements of the damage surface features (a daunting problem requiring human judgment and estimation due to typical damage site irregularity). Each damage site was characterized by measurements of mold impressions (damage depth, damage area) and was recorded on maps of damage site locations. Depth features as small as  $15\mu\text{m}$  (0.0006 inches) were recorded and mapped for further examination and analysis. The molds were measured with an optical comparator to determine damage size (cross-section and depth) at each impact site.

Stress analysis uses flaw depths in a static fatigue analysis that give a conservative estimate of the residual strength<sup>5</sup>. An assessment of remaining life was made in light of the residual strength and the pressure load encountered during launch, orbit, and reentry (glass loses strength when subjected to static stresses and pressure gradients<sup>6</sup>). On the basis of this analysis, a decision on window replacement was made.

As the Shuttle program progressed, studies of the effects of hypervelocity impacts continued for improvement of analytical approaches.<sup>7</sup> Hypervelocity impacts were made on silica blanks at the NASA Johnson Space Center Hypervelocity Impact Technology Facility (HIT-F) located at the White Sands Test Facility in Las Cruces, New Mexico. Generally, NASA defines hypervelocity impacts as impacts involving velocities greater than 5 km/s. Typically these impacts were made with a two-stage light-gas gun launcher. The impacts were made under various conditions, with the firings of impacters of various materials and at a variety of angles.

During the operations outlined in Reference 4, damages to shuttle windows other than from hypervelocity impacts have also been noted. Specifically bruises, a class of

(low velocity) impacts that cause underlying damage, do not create surface disruptions with the same characteristics of the damage accumulation associated with higher velocity impacts. Examples of the causes of this damage classification include the dropping of an object or tool onto the window and a tool swinging from a tether that collides with the windowpane during vehicle servicing. Still other damage includes the dragging of a dull object across the glass surface. This type of damage falls under a specific category, “chatter checks”, and is characterized by a linear series of small bruises of similar diameter caused by the friction contact between the glass and the object in contact with it.

The purpose of this work is to investigate and report on an alternative, more reliable, and more accurate inspection method with improved reliability for location and a predictive assessment of loss of fracture strength caused by windowpane damage in aerospace vehicles. Further, we compare the capability of this new technique with the currently used inspection techniques to predict loss of fracture strength. This new technique uses a Grey Field Polariscope (GFP) to measure stress birefringence<sup>8</sup>, the photoelastic response to stress fields in glass. When the glass is damaged, light waves passing through the damage regions have different velocities according to the local stresses associated with the damage and their alignments with the light’s polarization states. Hence, one easily locates and characterizes damage regions by noting locations and variations of light speed with polarization direction. Moreover, the photoelastic region surrounding the damage site extends over much larger distances than the damage site itself, thus making detection easier. Once located the photoelastic response determines the residual stress field around the damage site.

An orbiter window inspection system based on the GFP principle was designed and built to perform this inspection.<sup>9</sup> This scanning system allows single-sided inspection of windows and mounts to an x-y articulated translation mechanism capable of examining each windowpane in place and hence without the necessity of the pane’s removal from the vehicle. By combining the outputs from the GFP and the coordinate information this instrument makes an accurate map of damage site locations. The map includes coordinates, the optical image, and the strain patterns of each detected damage site for future reference, comparisons, and analysis, including differential analysis.

In this investigation, we test the ability of the GFP-based measurements to predict fracture strength on a series of specimens with damage sites that are cored from shuttle window material. Measurements were taken with a GFP inspection system at and near regions of damage caused by the four different damage classifications under test<sup>10</sup> (HVI, HIT-F, Bruises, and Chatter checks). The standard (depth and size) measurements taken during inspection are included in this study. We compare measurements of photoelastic retardation (*PER*) around damage sites and the standard measurements, and correlate these with the measured fracture strength<sup>11</sup> of the specimens. We develop an analytical model that suggests and outlines the basic aspects of a *PER* measurement procedure leading to the prediction.

We assume that *PER* is related to the residual stress field surrounding the damage site. The progenitor of the stress-field is the energy of the incoming collider or particle. Depending upon path and initial conditions the causes of fracture strength reduction are also related to the particle energy. Such colliding particle properties as coefficients of restitution, diameter, angle of impact, density, etc. also affect fracture strength of the window. We therefore derive an expression that relates fracture strength loss in the window as a result of a colliding particle to the energy imparted to the plastic strain in the glass at the damage site, which is then related to the measurement of the photoelastic response. This plastic strain at the damage site in turn causes an elastic stress field in the surrounding region measured with *PER*, which is then related to fracture strength through



the expression for the energy imparted to the plastic strain. We simplify the case by the limiting assumption that the particle speed is small enough that rate dynamics associated with glass impacts do not appreciably affect the outcome<sup>12</sup>. The *PER*, averaged around the damage site, is checked against the tested strength in shuttle glass specimens with damage. Data analysis confirms that the GFP, which is a nondestructive, non-contacting measurement system based on relating residual stress fields surrounding damage sites in glass to optical birefringence measurements, is more accurate than the other measurements used in this study in predicting fracture strength in annealed fused silica with damage (HVI and Bruises). This technique is less labor intensive, removes many ambiguities associated with the previously used characterizations, and is more accurate in predicting fracture strength degradation for HVI and Bruise damage.

## II. THEORY OF COLLISIONS OF PARTICLES WITH GLASS

This section is divided into four segments. The first segment considers the activation of a critical size flaw within the glass by a collision process. Specifically this is a derivation of the loss in strength of an annealed fused silica specimen caused by a collision with a particle, which we treat from the plastic deformation caused by a sequence of differential quasi-static indentations. The energy thus imparted has a multitude of paths that depend on parameters of the colliding particle at impact. These include material transformations, shock wave formations with consequent damage initiation, etc. The second segment derives a relationship from the output of the GFP to the strain field caused by the damage. The third segment develops the relationship between damaged glass fracture strength and the specific measurements from the GFP. In the fourth segment, we outline the foundation for a general experimental approach to nondestructively measure the parameters capable of predicting the fracture strength in annealed fused silica. This foundation is based on the analysis presented in the first three segments.

### IIA. Particle Collisions with Glass.

We begin the discussion with a particle of mass  $m$  moving toward and colliding with the windowpane fabricated from annealed fused silica. The particle velocity (relative to the window),  $u$ , is normal to the window surface. As it collides with the surface, the glass undergoes a deformation, of which part is plastic and part is elastic. In this case we are interested in the plastic component, as it contains a shift in the glass molecular structure, which causes a residual variation of index of refraction as a function of the polarization direction of light. We neglect rate-dependent processes and treat the collision as a series of differential quasi-static processes by time-sequencing an indentation caused by the colliding particle as the prototypical source of the damage<sup>13</sup>. We also assume that the colliding particle loses no mass as a result of the collision.

Consider a particle moving vertically toward the glass window, considered infinitely massive in this case, with a speed,  $u$ . The particle collides with the glass surface and rebounds with a speed  $v$ . The particle energy before collision  $T_{initial}$  is

$$T_{initial} = \frac{1}{2} mu^2 \quad (1)$$

After the rebound the particle energy  $T_{after}$  is



$$T_{after} = \frac{1}{2}mv^2 \quad (2)$$

The energy imparted to the glass,  $T$  is

$$T = T_{initial} - T_{after} = \frac{1}{2}mu^2(1 - e^2) \quad (3)$$

where  $e$  is the coefficient of restitution of the collision process associated with the deformation. If the collision is completely elastic, then  $e = 1$ . If the collision is completely inelastic, then  $e=0$ . In the case that we examine here,  $0 < e < 1$ . The remaining analysis considers what changes occur in the glass from the collision process. For this process, we specify the coefficient of restitution as being associated in part with the plastic deformation and its effects within the glass<sup>14</sup>.

We next examine the effects of the indenter's collision and consequent indentation of the glass surface. We simplify by assuming a completely rigid sharp indenter so that  $e$  represents the damage caused by the energy lost in the glass. Therefore, a portion of the kinetic energy of the indenter is dissipated by the mechanisms used for the local molecular rearrangement in the glass as the indenter penetrates into the glass. This rearrangement also causes an elastic residual field outside the damage site.

We begin from the perspective of indenting the surface. In this case hardness is the significant parameter. We start with a general definition of hardness, derive the energy deposition into the damage site, and analyze effects on strength by using fracture mechanics. Finally, we apply these results to effects on optical birefringence of glass, and deduce the connection between strength and photoelastic retardation measured with a modified grey-field polariscope.

Following an approach presented in Reference 2, Figure 1 is a schematic diagram of an idealized damage infliction with coordinates shown. The projectile tip formed by an angle of  $2\psi$  penetrates a distance  $z$  into the glass surface. The penetration profile on the glass surface is circular with a radius  $a$ . The penetration causes the formation of the plastic zone in the glass ahead of the projectile, which is treated as an indenter.

We begin with the geometrical relationship between the penetration profile and the indenter angle:

$$a = z \tan \psi \quad (4)$$

The mean stress  $p_{mean}$  is given by

$$H \equiv p_{mean} = \frac{F}{\Lambda \pi a^2} \quad (5)$$

where  $H$  is the hardness,  $F$  is the force exerted by the projectile on the glass, and  $\Lambda$  is a geometrical factor that depends upon the projectile's shape. We assume that the mean stress remains constant throughout the process. By combining Eq. (4) and (5) and solving for the force, we obtain

$$F(z) = (9\Lambda\pi H \tan^2 \psi) z^2 \quad (6)$$

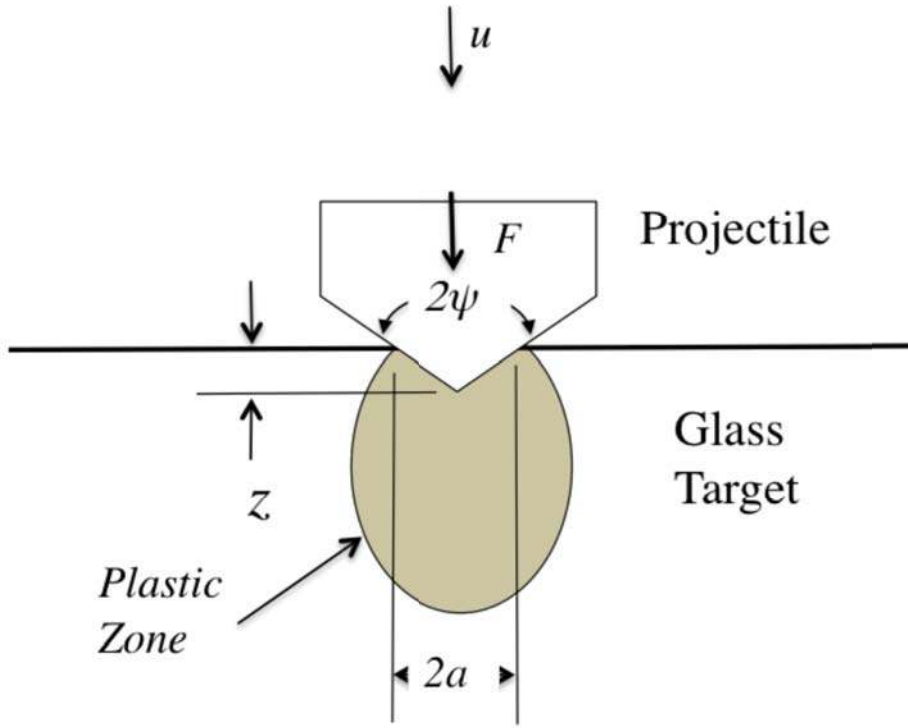


**Figure 1.** Diagram showing the projectile during collision with the glass target.

The work performed in forming the indentation in the glass is

$$W_{plastic} = \int_{z=0}^{z=z_m} F(z) dz = \frac{F_m^{3/2}}{(9\Lambda\pi H \tan^2 \psi)^{1/2}} \quad (7)$$

where  $F_m$  is force at maximum indentation.

We equate the kinetic energy of the projectile imparted to the glass (impact energy),

$$T = \frac{1}{2} mu^2(1 - e^2) \quad (8)$$

to the plastic work done when penetrating the glass, and solve for the force

$$F_m = (9\Lambda\pi H \tan^2 \psi)^{1/3} T^{2/3} \quad (9)$$

The dynamics of crack evolution from a stress caused by a sharp contact are covered elsewhere<sup>15</sup>. As the indenter penetrates the glass surface, a tensile stress concentration builds at the elastic-plastic interface, which extends outward from the impact site. At some critical force,  $F_{critical}$ , a subsurface flaw located within the field will experience sufficient stress over a large enough portion of the flaw that it will become unstable<sup>16</sup>. The critical force at which this occurs is

$$F_{critical} = \frac{\alpha_{e/p} K_c^4}{H^3} \quad (10)$$

where  $\alpha_{e/p}$  is an empirical factor that depends upon the indenter and the glass target, and  $K_c$  is the fracture toughness of the glass. This condition represents a minimum condition for crack initiation. The cracks thus initiated expand as half pennies centered at the point of impact and normal to the impact surface.

From fracture mechanics<sup>17</sup> one obtains a relationship between the crack depth,  $D$ , and the force exerted by the projectile (indenter) on the glass.

$$\frac{F}{D^{3/2}} = \xi_F K_c \quad (11)$$

where  $\xi_F$  is another empirical factor related to the projectile. The relationship between the maximum tensile stress (tensile strength  $\sigma$ ) and the dominant flaw length  $l_{flaw}$  is given by

$$\sigma = \frac{K_c}{(\pi l_{flaw})^{1/2}} \quad (12)$$

Below threshold speeds,  $u_0$ , no damage greater than flaw lengths that are already present in the glass is created. Above speeds of  $u_0$  an indentation flaw (crack) of length  $D$  dominates the maximum tensile strength. Hence we write the dominant flaw length in the two cases:

$$\begin{aligned} l_{flaw} &= l_{0,flaw}, & u < u_0 \\ l_{flaw} &= \Omega D, & u > u_0 \end{aligned} \quad (13)$$

where  $\Omega$  is a geometric constant ( $4/\pi^2$  for penny cracks<sup>18</sup>). The fracture stress (strength)  $\sigma_{fracture}$  then becomes

$$\sigma_{fracture} = \frac{K_c}{(\pi l_{flaw})^{1/2}} \quad T < T^* \quad (14a)$$

$$\sigma_{fracture} = \left[ \left( \frac{1}{9\pi^{11/2}} \right)^{1/9} \left( \frac{\xi_F^3}{\Lambda \tan^2 \psi} \right)^{1/9} \left( \frac{K_c^{4/3}}{\Omega^{1/2} H^{1/9}} \right) \right] T^{-2/9} \quad T > T^* \quad (14b)$$

For the data presented here we consider the case of where  $T > T^*$ , where  $T^*$  is a minimum energy below which damage is not added to the glass. As outlined in the derivation the impacts of high velocity particles with the glass surface causes localized damage sites that affect the glass target's fracture strength.

Several observations from the derivation may be made at this point. First, some collisions below a threshold energy, even though they may cause plastic deformations, do not appreciably alter glass strength, since any crack formed does not exceed naturally occurring flaw lengths already in the glass. Secondly, as the particle impact speed

increases within a range above a minimum speed (determined by the threshold energy), the fracture strength decreases inversely with impact energy to the  $2/9$  power. Thirdly, one generalizes the impact process by noting that any energy imparted to the glass, including the work of dragging a blunt object across the surface, can suffice in causing damage that results in a decrease in fracture strength. Regardless of the damage source, damage accumulation that affects strength results in the displacement of atomic arrangements within the glass volume. Therefore any inspection method that responds to displacement of material arrangements in glass, even at the atomic level, is useful in assessing changes in the fracture strength of glass.

To gain insight into collision damage, an X-ray computed tomography was made of a damage site (one of several sites) in a specimen cut from a shuttle window.

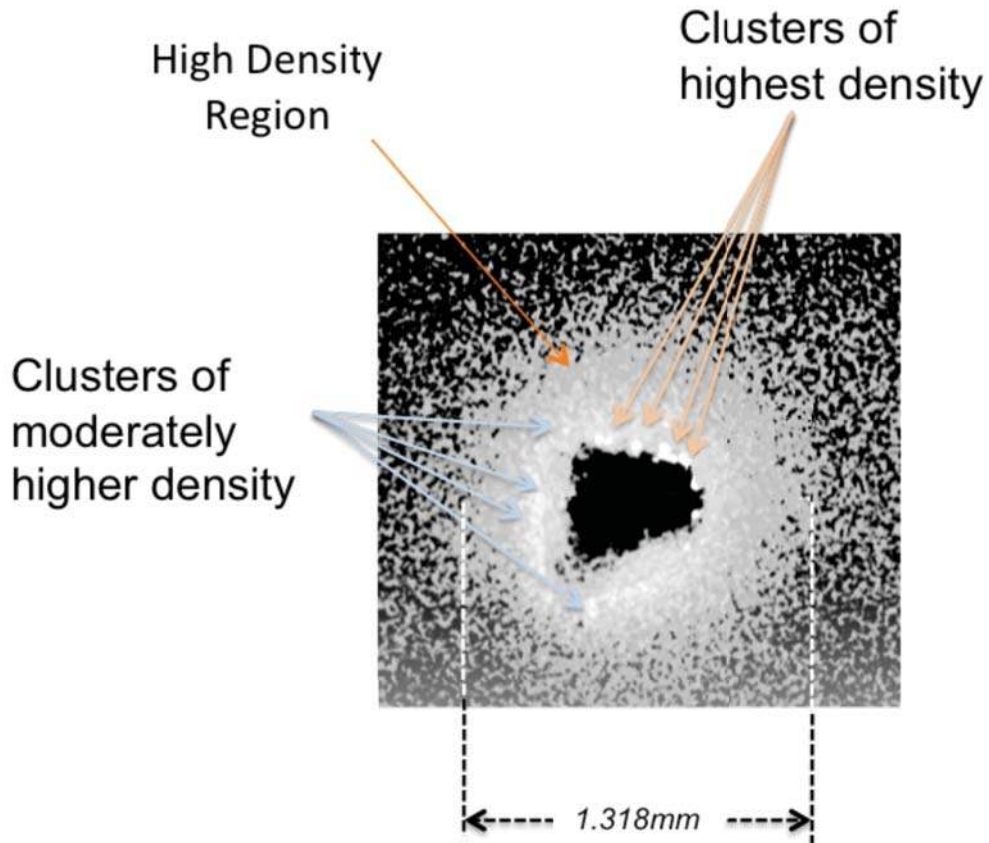


**Figure 2.** An X-Ray tomographic view (slice) of a damage site in shuttle glass specimen 27-165. Within the region of this slice are characteristics showing regions of differing density to x-ray transmission. It is thought that this slice shows a compressive stress field that surrounds the damage site.

Figure 2 is a slice of the x-ray computed tomographic image (negative presentation), which shows the damage in a plane within the fused silica shuttle glass specimen. In this presentation, lighter regions indicate more x-ray absorption, where darker regions indicate relatively less x-ray absorption. The slice shown is relatively close to the surface where some material has been knocked away, and thus leaves a void (black center). The region surrounding the black center extends a distance of 1.3 mm edge-to-edge (a factor of  $\sim 2.7$  larger than the void) and shows a higher density (indicated in the image by lighter shades and shading). Marked on the diagram are regions of various densities. Extending from the perimeter of the damage site outward into the material is a diffused increase in density over the background, thus possibly indicating a region of some strain.

A zone of demarcation is outlined by the slightly brighter regions marked by clusters of moderately higher density. Between the demarcation zone and the black interior are regions with clusters of highest density. This diagram is consistent with compressive stress fields surrounding the damage site.

While manufacturing techniques vary, fused silica is a super-cooled state of melted silicon dioxide (silica) with various levels of impurities and, depending on application, additives. Without additives it is an amorphous structure of silicon dioxide, another form of which is crystalline quartz.

Fused silica is in a configurational state with higher energy than the lowest energy for silica, a quartz state,  $\alpha$ -quartz.  $\alpha$ -quartz is a trigonal trapezohedral crystal class 3 2, or crystalline form. Other forms include  $\beta$ -quartz, which includes a hexagonal 622 form with melting points of 1670C [ $\beta$  tridymite] and 1713C [ $\beta$  cristobalite]. Both  $\beta$  forms have configurational energies above  $\alpha$ -quartz, but lower than amorphous silica. Because of the high activation energies of the different forms of silica, it is possible for these forms to be present in metastable states<sup>19</sup> even at standard temperatures and pressures. Since local energy densities from the impact are quite high, it may be energetically possible that silica progresses locally (at the atomic level) from the amorphous state to other forms (as might be included in the density changes shown in the X-ray CT in Figure 2) when damaged. Regardless of whether the impact, which causes local atomic rearrangements, is the source, or the extended (elastic) stress field is the source, the birefringent properties of fused silica offer the possibility of a quantitative assessment and characterization of these fields.

### **IIB. Principle of grey-field photoelasticity.**

We next measure the effect of stress fields left in the glass by the impact. The process that we use is governed by the fact that regions surrounding damage sites in glass become photo-responsive to polarized light. The degree of responsiveness is directly related to the magnitude and extent of the plastic stress field and the elastic stress field that extend beyond the immediate damage site. The first stress field is close to the damage site, and is largely due to plastic –related effects in the glass from the projectile, which affect local volume. Away from the damage site there is an elastic stress field caused by this volume change. This field extends for some distance from the damage site.

The visible light GFP was originally developed by Stress Photonics, Inc. for NASA<sup>20</sup> to provide high-resolution full-field subfringe photoelastic stress analysis in materials transparent to visible light<sup>21</sup>. In photoelasticity, the stress field of a test article is evaluated through the use of polarized light. The GFP performs this evaluation by combining a circularly polarized light source with a linearly polarized analyzer. As the analyzer is rotated, data is acquired with a video camera that uses synchronous (synchronized with the rotation of the analyzer) demodulation.

Figure 3 shows a schematic representation of grey-field polariscope using photoelasticity to inspect a specimen that exhibits birefringence when strained. Circularly polarized light is represented by two orthogonal linear polarized light vectors that are out of phase by  $\pi/2$  radians.

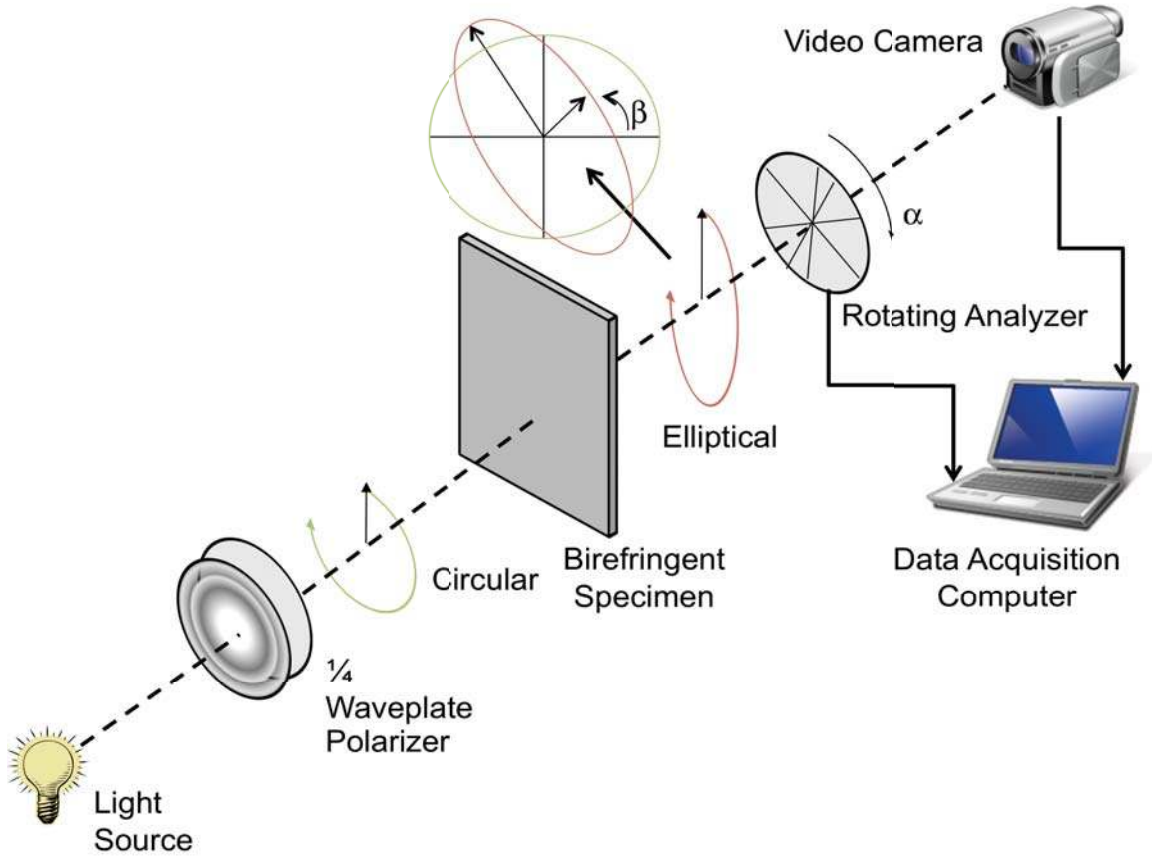


**Figure 3.** Schematic representation of the grey-field polariscope.

It has been shown by Horn<sup>22</sup> that for the GFP configuration described above, the intensity of the transmitted light is:

$$I = \kappa_E A^2 (1 + \sin\{2(\alpha - \beta)\} \sin\Delta) \quad (15)$$

where  $A$  is amplitude of the circularly polarized light,  $\alpha$  is the angular orientation of the analyzer,  $\beta$  is the orientation of the fast axis of the resulting elliptical light,  $\Delta$  is the phase lag of the slow axis of the ellipse due to the stress-birefringence of the specimen, and  $\kappa_E$  is a constant of proportionality. When  $\alpha - \beta = 0$ , the intensity  $I = \kappa_E A^2$ . This condition marks the alignment of fast-axis orientation with the analyzer angle ( $\alpha = \beta$ ). When  $\alpha - \beta$  is  $\pm 45^\circ$  the intensity  $I = \kappa_E A^2 (1 \pm \sin\Delta)$ , which determines  $\Delta$  experimentally.

For the elastic case of birefringent retardation we define  $\Delta$ ,

$$\Delta = \frac{2\pi Cl}{\lambda} (\sigma_1 - \sigma_2) \quad (16)$$

where  $C$  is the elastic stress-optic coefficient,  $\lambda$  is the wavelength of the light,  $l$  is the thickness of the plate and  $\sigma_1$  and  $\sigma_2$  are the first and second principal stresses<sup>23</sup>.

The damage site specifically will have a plastic rearrangement of atomic structures around the damage site, and a region (far field) surrounding the damage site where atomic position shifts are elastic. This study utilizes the elastic stress field for analysis.

By dividing Eq. (15) by  $\kappa_E A^2$ , and using a trigonometric identity to rewrite the RHS in terms of the angular orientation  $\alpha$ , one obtains

$$\frac{I}{\kappa_E A^2} = 1 + I_{ca} \cos 2\alpha + I_{sa} \sin 2\alpha \quad (17)$$

where the (dimensionless) normalized intensities are

$$I_{ca} = -(\sin \Delta) \sin 2\beta \quad (18a)$$

$$I_{sa} = (\sin \Delta) \cos 2\beta \quad (18b)$$

and  $\Delta$  is the birefringent or photoelastic phase retardation,  $PER_\phi$ .

The first principal stresses are related directly to the sine and cosine amplitudes ( $I_{ca}$ ,  $I_{sa}$ ) by

$$\sin \Delta = \sqrt{I_{ca}^2 + I_{sa}^2} \quad (19)$$

$$\beta = \frac{1}{2} \tan^{-1} \left( -\frac{I_{ca}}{I_{sa}} \right) \quad (20)$$

For most applications of interest the shear stresses encountered are small. Therefore the  $PER_\phi$  are small (subfringe). Equation (19) can be simplified further by using the relationship  $\sin \Delta \approx \Delta$ . We combine this with Equation (16) to give:

$$(\sigma_1 - \sigma_2) = \frac{\lambda}{2\pi Cl} \sqrt{I_{ca}^2 + I_{sa}^2} = \frac{\lambda}{2\pi Cl} PER_\phi \quad (21)$$

Horn gives a geometric interpretation of Eq. (21) by using a Mohr's circle<sup>24</sup>, with a radius of  $(\sigma_1 - \sigma_2)/2$  for the case of elastic deformation. This allows for the following relationships to be directly developed from the sine and cosine intensities ( $I_{sa}$  and  $I_{ca}$  respectively) discussed above:

$$I_{sa} \propto (\sigma_{xx} - \sigma_{yy}) \quad (22)$$

$$I_{ca} \propto \tau_{xy} [= (\sigma_{+45} - \sigma_{-45})] \quad (23)$$

The analysis for the elastic case was generated for the commercially developed unit, currently marketed by Stress Photonics<sup>20-23</sup>. This laboratory instrument is a transmission system that has a spatial resolution determined by the diffraction limits of the lens system.

### **III.C. The relationship between collision dynamics and photoelastic retardation measured in this study.**

When silica is in the annealed amorphous state, it is not birefringent. As stresses increase, there becomes a directional dependence of the electric field vector's speed of propagation through the glass. Since impacts cause plastic (irreversible) deformation



(leading to crack formation) around the impact site, there is a residual stress field and an accompanying  $PER_\phi$  surrounding the damage site. The birefringence begins at the periphery of the damage site affected zone, and increases as the stress increases, throughout the damage zone of depth  $l$ .

Damage sites in orbiter windows always occur on the outer surface of the window. Where impact occurs, the surrounding volume becomes stressed, while the remaining material beneath the damage zone is less affected. Figure 4 (ahead in Section IID) shows a schematic of an impact site cross-section, where regions near the center show compressions as indicated by the increased density to x-radiation (Figure 2. An elastic residual stress field surrounds the impact site and extends radially for a substantial distance into the elastic zone.

Consider a ray of circularly polarized light passing through the stress field surrounding the damage site as shown in Figure 4. Since the extent of the residual stress field (and hence  $PER_\phi$ ) is related to the impact energy, we assume that the fracture strength varies (as shown in the low velocity impact case) with the amplitude of the  $PER_\phi$  (averaged around a path in the elastic zone). Therefore, the magnitude of the  $PER_\phi$  as averaged around the damage site in this study, is experimentally shown to be an indicator of breakage strength. The plastic deformation from the damage affects  $PER_\phi$  in the elastic zone. In turn, the  $PER_\phi$ , which is related to the principal stresses at each point in the stress field, is related to the impact energy.

In this section we outline the mechanisms and derive expressions that relate the  $PER_\phi$  associated with the stress pattern in the elastic region, where Equation (16) applies, to the plastic deformation at the collision site. We model the formation of the plastic (damage) zone by a network of radially oriented edge dislocations, each with a Burgers vector of  $b$ , which we represent as a set of dislocations that are aligned in a uniform, radially symmetric pattern about the origin. We define an effective Burgers vector to represent the effect of the plastic deformation on the stress fields. We write plane stress fields in the elastic region. We recast  $PER_\phi$  to  $PER$  (with units of nanometers) to correspond with experimental measurements. We use Mohr's Circle analysis to determine the relationship of  $PER$  to principle stress fields at each point in the elastic stress field. We sum  $PER$  contributions to each illuminating ray, passing near the damage-affected zone, and parallel to the damage axis. Then we perform an integral of  $PER$  at points on a circular path with the plastic zone site at the center, and relate this to a product,  $Nbl$ , which is a measure of the plastic deformations inflicted at the damage site. From this analysis, we construct an experimental procedure to measure this product, and apply these measurements to the four classes of inflicted damage to orbiter windowpanes. We write an energy expression for the plastic zone and relate it to the energy of the incoming particle and the  $PER$  measurements in the elastic field. Finally, we apply the previous analysis to predict fracture strength based on the  $PER$  measurements.

Consider that the plastic deformation zone results from a process where atomic planes are forced in a close-packed configuration until the penetrating particle energy is dissipated<sup>25</sup>. We model the process as the generation of fields of edge dislocations with the extra planes inserted radially outward from the impact site, and distributed throughout the damage-affected volume. Let the number of edge dislocations inserted be  $N$ , so that the number of dislocations between  $\theta$  and  $\theta+d\theta$  equals  $(N/2\pi)d\theta$ . The Burger's vector contribution to the stress field between  $\theta$  and  $\theta+d\theta$  is then  $(Nb/2\pi) d\theta$ . Adopting the hollow core model<sup>26,27</sup> of Volterra, we write the elastic-zone stress in cylindrical coordinates by summing the distribution of Burger's vectors contributions to the stress fields. At a distance  $r$  from the z-axis (in cylindrical coordinates)<sup>28</sup>,

$$\sigma_{rr} = \sigma_{\theta\theta} = \int_{\theta=-\frac{\pi}{2}}^{\theta=\frac{\pi}{2}} \frac{-GNb}{4\pi^2(1-\nu)r} \sin\theta d\theta = 0 \quad (24)$$

$$\sigma_{r\theta} = \int_{\theta=-\frac{\pi}{2}}^{\theta=\frac{\pi}{2}} \frac{GNb}{4\pi^2(1-\nu)r} \cos\theta d\theta = \frac{GNb}{2\pi^2(1-\nu)r} \quad (25)$$

where  $G$  is the shear modulus,  $\nu$  is Poisson Contraction. Calculation of Mohr's Circle parameters from these values gives a center location,  $\bar{\sigma}$ , and radius  $R$ , respectively, of

$$\bar{\sigma} = \frac{\sigma_{rr} + \sigma_{\theta\theta}}{2} = 0 \quad (26)$$

$$R = \sqrt{\left(\frac{\sigma_{rr} - \sigma_{\theta\theta}}{2}\right)^2 + \sigma_{r\theta}^2} = \frac{GNb}{2\pi^2(1-\nu)r}$$

The instrument measures the photoelastic retardation  $PER$  in units of nanometers. From Equation (16) we write

$$PER = \frac{\lambda}{2\pi} PER_{\phi} = \frac{\lambda}{2\pi} \sqrt{I_{ca}^2 + I_{sa}^2} \quad (27)$$

$$PER = \sqrt{I_{ca, nm}^2 + I_{sa, nm}^2}$$

where  $I_{ca, nm}$  and  $I_{sa, nm}$  are  $I_{ca}$  and  $I_{sa}$  respectively, converted to nanometers. Substituting  $2R$  for the principal stress differences,  $\sigma_1 - \sigma_2$ , into Equation (21), then substituting in Equation (27), and solving for  $Nb$  gives

$$Nb = r \frac{\pi^2 (1-\nu)}{Cl} \frac{1}{G} \sqrt{I_{ca, nm}^2 + I_{sa, nm}^2} \quad (28)$$

Next we average  $\sqrt{I_{ca, nm}^2 + I_{sa, nm}^2}$  around the circumference of radius  $\zeta$  chosen for measurement. This averaging is to compensate for asymmetries that may be encountered in the damage sites.

$$\left\langle \sqrt{I_{ca, nm}^2 + I_{sa, nm}^2} \right\rangle = \frac{1}{2\pi} \int_{\theta=0}^{\theta=2\pi} \sqrt{I_{ca, nm}^2 + I_{sa, nm}^2} d\theta \quad (29)$$

Solving for  $\langle Nb \rangle l$  gives an average value over the path of measurement

$$\langle Nb \rangle l = \xi \frac{\pi^2 (1-\nu)}{GC} \left\langle \sqrt{I_{ca, nm}^2 + I_{sa, nm}^2} \right\rangle \quad (30)$$

Equation (30) shows that, for any experimental set-up to measure  $PER$ , the measurements of radius  $\zeta$ , the material properties,  $\nu$ ,  $G$ , and  $C$ , one can determine a property of the

plastically deformed volume represented by the product,  $\langle Nb \rangle l$ . For any damage site, one can assume that  $\langle Nb \rangle l$  remains fixed, so the measurement of *PER* averaged around the radius  $\xi$  is directly proportional to the accumulated plastically stressed material.

Recalling Equation (7), we calculate the indentation depth from

$$W_{plastic} = \int_{z=0}^{z=l_p} (\Lambda\pi H \tan^2 \psi) z^2 dz = (\Lambda\pi H \tan^2 \psi) \frac{l_p^3}{3} \quad (31)$$

where  $l_p$  is the indentation depth. We assume that  $l_p$  is related to the compression beneath the collision to give an effective damage length<sup>29</sup>, which we equate to the damage zone depth  $l$ , where  $l = \kappa l_p^\xi$ . We equate  $W_{plastic}$  to the plastically deforming component of the collision particle energy,  $T$ , given in Equation (8) and solve for  $l$  to obtain

$$l = \left( \frac{3\nu\kappa^{\frac{3}{\xi}} T}{\Lambda\pi H \tan^2 \psi} \right)^{\frac{\xi}{3}} \quad (32)$$

where  $\nu$  is the fractional component of the particle energy imparted to the glass,  $T$ , utilized in the plastic deformation processes. We assume the compressed region below the indentation also contributes to the effective distance  $l$  and hence the cumulative *PER*. Combining with

Equation (30) we solve for  $\langle Nb \rangle$

$$\langle Nb \rangle = \xi \frac{\pi^2(1-\nu)}{GC} \left\langle \sqrt{I_{ca,nm}^2 + I_{sa,nm}^2} \right\rangle \left( \frac{3\nu\kappa^{\frac{3}{\xi}} T}{\Lambda\pi H \tan^2 \psi} \right)^{\frac{\xi}{3}} \quad (33)$$

The derivation above identifies the variables and parameters so that an experimental procedure can be developed to measure the quantities shown in Equation (33), and related to the fracture strength. We include contributions to *PER* from plane stresses that exist well below the disruption zone normally measured with other optical instruments such as microscopes including those with special illumination features. The extent of the increase of *PER* from the region below the disruption zone is not examined here. This area is one for future exploration and experimental confirmation. Using the results of Equation (33) in Equation (14b) we get the dependency of the fracture strength of glass in terms of *PER* measured in this investigation.

$$\left\langle \sqrt{I_{ca,nm}^2 + I_{sa,nm}^2} \right\rangle = PER = \frac{\langle Nb \rangle GC}{\xi \pi^2(1-\nu)} \left( \frac{3\nu\kappa^{\frac{3}{\xi}} T}{\Lambda\pi H \tan^2 \psi} \right)^{\frac{\xi}{3}} T^{\frac{\xi}{3}} \quad (34)$$

Combining the constants and solving for  $T$  gives

$$\Xi = \frac{\langle Nb \rangle GC}{\xi \pi^2 (1 - \nu)} \left( \frac{3 \nu \kappa^{\frac{3}{\zeta}}}{\Lambda \pi H \tan^2 \psi} \right)^{\frac{\zeta}{3}} \quad (35)$$

$$T = \left( \frac{PER}{\Xi} \right)^{\frac{3}{\zeta}}$$

Substituting into Equation (14b) gives the relationship between the fracture strength and  $PER$  as

$$\sigma_{fracture} = A(PER)^{-\frac{2}{3\zeta}}$$

$$\sigma_{fracture} = \left[ \left( \frac{1}{9\pi^{11/2}} \right)^{1/9} \left( \frac{\xi_F^3}{\Lambda \tan^2 \psi} \right)^{1/9} \left( \frac{K_c^{4/3}}{\Omega^{1/2} H^{1/9}} \right) (\Xi)^{\frac{2}{3\zeta}} \right] (PER)^{-\frac{2}{3\zeta}} \quad (36)$$

While this equation was derived under the assumption that the indenter was of uniform shape as outlined in Section IIA, we extend the approach by noting that  $\zeta$  is expected to change for each class of damage accumulation, whether caused by a colliding particle or an indentation from another object. Some of this change is due to various shapes and sizes of indenter. Other parameters expected to alter  $\zeta$  include speed, impact angle, etc.

Each class of collision will have a value of  $\zeta$  because each path classification will have a differing plastic deformation associated with the path<sup>30</sup>. The effect on the prediction of fracture strength depends upon what path is followed.

### III. Energy Considerations in the Elastic Zone Stress Field

The general expression for the energy density  $U_0$  for a stress field in an isotropic material is written as

$$U_0 = \frac{1}{2E} (\sigma_{xx}^2 + \sigma_{yy}^2 + \sigma_{zz}^2) - \frac{\nu}{E} (\sigma_{xx}\sigma_{yy} + \sigma_{yy}\sigma_{zz} + \sigma_{zz}\sigma_{xx}) + \frac{1}{2G} (\tau_{xy}^2 + \tau_{xz}^2 + \tau_{zy}^2) \quad (37)$$

For the plane stress case we obtain the following in cylindrical coordinates

$$U_0 = \frac{1}{2E} (\sigma_{rr}^2 + \sigma_{\theta\theta}^2) - \frac{\nu}{E} (\sigma_{rr}\sigma_{\theta\theta}) + \frac{1}{2G} (\tau_{r\theta}^2) \quad (38)$$

Writing the energy density in terms of principal stresses using Mohr Circle parameters we obtain

$$\begin{aligned}
U_0 &= \frac{1}{2E}[(\bar{\sigma} + R)^2 + (\bar{\sigma} - R)^2] - \frac{\nu}{E}[\bar{\sigma}^2 - R^2] \\
&= \frac{1}{2G} \left[ R^2 + \left( \frac{1-\nu}{1+\nu} \right) \bar{\sigma}^2 \right]
\end{aligned} \tag{39}$$

where  $R = \sqrt{(\sigma_{rr} - \bar{\sigma})^2 + \tau_{r\theta}^2}$ , and  $E = 2G(1 + \nu)$ . Applying Equation (39) to the elastic zone for this case gives

$$U_0 = \frac{R^2}{2G} \tag{40}$$

Substituting the value for R from Equation (26) gives an expression for energy density in the elastic stress field of

$$U_0 = \frac{GN^2b^2}{8\pi^4(1-\nu)^2r^2} \tag{41}$$

Integrating over the elastic volume one obtains the energy stored in the elastic stress field,

$$U_{elastic} = \int_{r=r_{ref}}^{r=R_{max}} \frac{GN^2b^2}{8\pi^4(1-\nu)^2r^2} (2\pi r l dr) = \frac{GN^2b^2l}{4\pi^3(1-\nu)^2} \ln \frac{R_{max}}{r_{ref}} \tag{42}$$

where  $R_{max}$  in this application is the maximum extent of a measurable *PER*, and  $r_{ref}$  is the radius at the boundary between the elastic and plastic zones. Next one writes the maximum energy available for plastic compression as

$$U_{plastic} = T - U_{elastic} \tag{43}$$

where, as before, other modes of energy transformations are assumed to be small by comparison. The particle energy spent on plastic deformation, equal to  $U_{plastic}$ , can be estimated using Equation (32) for  $l$  in Equation (42). Then Equation (43) is written as

$$U_{plastic} = T - \left( \frac{GN^2b^2}{4\pi^3(1-\nu)^2} \ln \frac{R_{max}}{r_{ref}} \right) \left( \frac{3\nu\kappa^{\frac{3}{\zeta}}T}{\Lambda\pi H \tan^2\psi} \right)^{\frac{\zeta}{3}} \tag{44}$$

This estimate establishes the variables that affect plastic damage formation in the glass in terms of glass properties and particle energy and path characteristics. Substituting the measurements from GFP, and factoring gives

$$U_{plastic} = T^{\frac{\zeta}{3}} \left( T^{\frac{3+\zeta}{3}} - \frac{\pi\xi^2}{4GC^2} \chi^{\frac{\zeta}{3}} \langle I_{ca, nm}^2 + I_{sa, nm}^2 \rangle \ln \frac{R_{max}}{r_{ref}} \right) \tag{45}$$

where

$$\chi = \frac{3\nu\kappa^{\frac{3}{2}}}{\Lambda\pi H \tan^2 \psi} \quad (46)$$

### III. Experimental Design

Damage sites in orbiter windows always occur on the outer surface of the window. Where impact occurs, the surrounding volume becomes stressed, while the remaining material beneath the damage zone is less affected. Figure 4 shows a schematic of an impact site cross-section, where regions near the center show compressions as indicated by the increased density to x-radiation (Figure 2). An elastic residual stress field surrounds the impact site and extends radially for a substantial distance into the elastic zone.

Since the extent of the residual stress field (and hence  $PER_\phi$ ) is related to the impact energy, we assume that the fracture strength varies (as shown in the low velocity impact case) with the amplitude of the  $PER_\phi$  (averaged around a path in the elastic zone). Therefore, the magnitude of the  $PER_\phi$  as averaged around the damage site in this study, is experimentally shown to be an indicator of breakage strength. The plastic deformation from the damage affects  $PER_\phi$  in the elastic zone. In turn, the  $PER_\phi$ , which is related to the principal stresses at each point in the stress field, is related to the impact energy.

Consider a ray of circularly polarized light passing through the fused silica and into the damage-affected zone of depth  $l$ . Referring to the diagram in Figure (4) the measurement arrangement is shown on a fused silica specimen with a damage site extending from the specimen surface and into the specimen. Close to the impact surface the stress field begins to contribute to the photoelastic retardation. The damage-affected volume consists of a plastic zone, characterized by effects of the damage from the collision process, and an elastic zone which extends for a large distance from the site. This is labeled as the "*Damage-affected volume*" in the diagram. We examine and measure the cumulative effect on the ray from the birefringence caused by the residual stress field, which is in the "*Elastic Zone*" and radially outward from the "*Plastic Zone*" caused by the particle collision energy. The "*Circularly Polarized Ray*", parallel to the damage site axis and passing through the "*Measurement Circumference*" is well within the elastic zone and lies on the cylindrical surface defined by the *Measurement Circumference* and damage depth  $l$ . Since fused silica is optically inactive until subjected to stress, the ray is only affected at and near the elastic portion of the damage-affected zone. By examination of Equation (30) we note that averaging the measured  $PER$  at any radius around the damage site center, one obtains a quantity which is proportional to the damage within the damage volume. Since this is the case, the experimenter may choose any radius that is experimentally convenient, without appreciably affecting the analysis.

As the circularly polarized ray passes into and through the damage-affected elastic zone, it accumulates retardation effects of the stress on the wave speed of the light polarized in the direction of the compression. The ray emerges from the glass along with the direction-dependent polarization retardations, which gives a phase shift between the different polarization directions. The rotating analyzer and video imaging system with appropriate software decodes the phase shift into the retardation ( $PER$ ) and records it as

part of an image. For each damage site *PER* was calculated and compared with breakage strength.

In the experimental design used to collect data for this paper, we kept the measurement radius constant and sufficiently large so that the circumference was always larger than the plastic damage zones<sup>31</sup> for all damage sites except chatter checks<sup>32</sup> Measurements of *PER* were taken and averaged around the measurement circumference, as shown in the diagram. The measurement technique was applied to damage sites of different damage classifications.

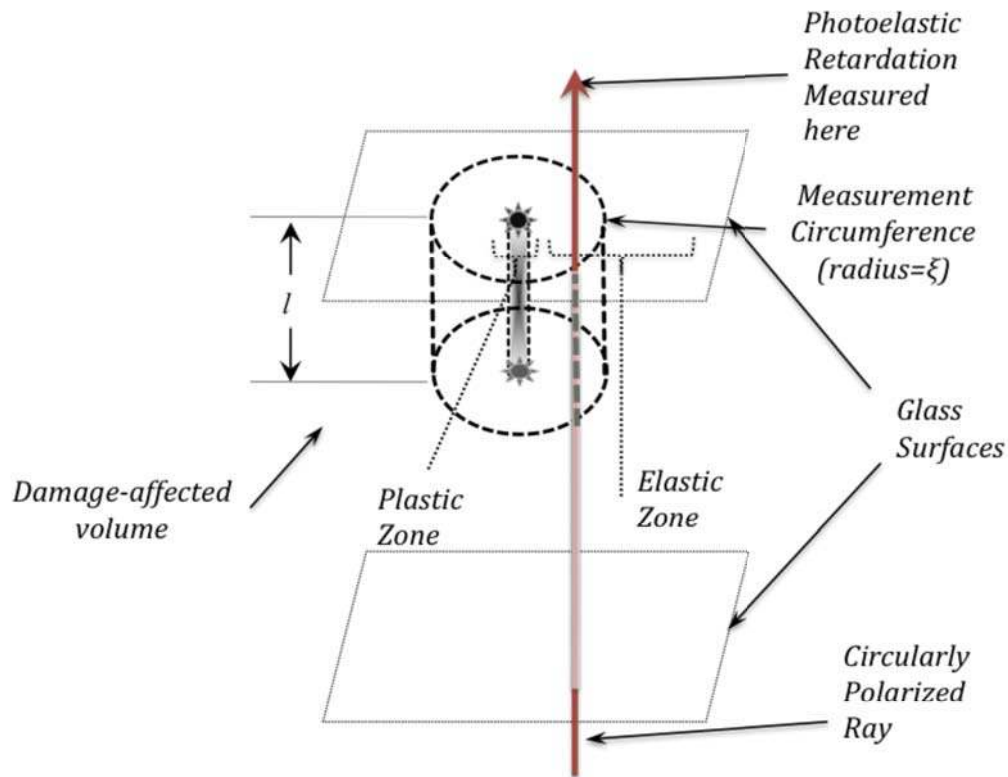


**Figure 4.** A schematic diagram of the elements to illustrate the technique for measuring the photoelastic retardation around a damage site in fused silica. The measurement is made in the elastic zone.

### III. MEASUREMENTS AND ANALYSIS

Specimens were prepared from windows taken from shuttle vehicles. The four general classes of damage in this study are (1) *HVI*, hyper velocity impacts encountered during shuttle flight, (2) *HIT-F*, lab created hypervelocity impacts from uniform shaped projectiles at the Hypervelocity Impact Technology Facility, (3) *Bruises*, impacts from low-velocity masses, and (4) *Chatter Checks*, a linear series of bruises inflicted by dull and slow objects moving across the glass surface. Specimens from each class were measured with various tools to record the size and the depth of the damage site. Measurements were also taken with the grey-field polariscope images using a Stress Photonics, Inc. device (GFP 2400 Camera) to determine the *PER* and to obtain an image of the damage site in circular polarized light. Then the specimens were broken to measure the fracture strength.



We use the standard methods to analyze empirical data: the linear fit, the two semi-log fits (logarithm and exponential, depending on axis orientation), and the log-log plot or power law fit. The linear fit is given by the form ( $y=Bx+A$ ). Similarly, the exponential fit is given by ( $y=Ae^{Bx}$ ); The log fit is given by ( $y=A+B\log x$ ); and the power-law fit is given by ( $y=Ax^B$ ). In these cases,  $y$  is the fracture strength.

From the extensive records kept on each window, natural *HVI* sites that occurred during shuttle missions were identified and cored from retired windowpanes. Protection was provided at the damage site with cardboard and tape or suction cups. Then the pane was placed on a water knife where the core was removed, leaving the remaining pane (the “carcass”) undamaged. The core diameter was dictated by parameters provided in the ASTM1499-C specification for ring-ring bi-axial strength testing. The remaining parts of pane carcasses could then be inflicted with other classes of damage for testing.

HIT-F #	Projectile Material	Projectile Diameter (mm)	Shot Velocity (km/s)	Impact Angle (deg)	Surface damage X (mm)	Surface damage Y (mm)	Depth of crater (mm)
HITF05186	GLASS	0.2	4.16	60	3.1	3.7	0.12
HITF05190	ALUMINUM	0.2	6.82	45	5.0	5.4	0.25
HITF05195	ALUMINUM	0.2	4.04	60	2.15	2.5	.1
HITF05202	GLASS	0.1	6.81	60	1.4	1.9	0.04
HITF05305	SAPPHIRE	0.2	5.03	0	4.7	4.5	0.4
HITF05310	SAPPHIRE	0.2	6.91	60	6.5	7	0.22
HITF05314	STEEL	0.25	4.97	0	10.7	9.4	0.72
HITF05329	GLASS	0.05	4.0?	45	0.34	0.33	0.03
HITF03021	ALUMINUM	0.6	7.06	0	27.5*	27.5*	1.950
HITF03051	ALUMINUM	0.4	6.88	0	16*	16*	1.220

**Table 1.** Data from *HIT-F* collisions. Included are parameters associated with the collisions, and measurements of surface damage. Not shown in this table are the photoelastic retardation measurements. \* indicates that measurement is a diameter.

In the *HIT-F* case, the inflicted damage came from colliding projectiles fired from a light gas gun at the Hypervelocity Impact Technology Facility at the White Sands Test Facility (Las Cruces, NM). The projectile mass, profile, and speed were controlled and measured. The projectile materials, sizes, velocities, and angles of impact for some of the *HIT-F* specimens included in this research are provided in Table 1.

For the *Bruise* category, each specimen was damaged by dropping various sized metal bearings on the glass, causing low-speed (Hertzian) impacts to the pane surface. The bearing drop was controlled by rolling it down a metal channel with one end placed a prescribed distance from the surface of the glass. Various impact velocities (not measured or recorded) were obtained by placing the bearings at various distances up the channel for release. This category of damage is intended to simulate dropped items on the window during servicing of the vehicle.

The last damage type, *Chatter Checks*, was formed by placing a sheet of paper on the glass and simply drawing a line on that sheet with a ball-point pen. The metal ball of the pen produced enough friction between the glass and paper to inflict remarkably consistent width chatter checks. The lengths of the chatter checks were varied, as this was (erroneously) thought to be the controlling feature for strength. The chatter check category simulates damage that might be inflicted during storage and preparation for flight. Of all the damage inflicted, the chatter check damage type appeared to cause the least damage.



**Figure 5.** Experimental arrangement set-up for inflicting bruise damage on glass panes.

Once the bruises and chatter checks were inflicted on the windowpane carcasses, the panes were shipped to Southwest Research Institute for measurements of breakage strength. Similar to the HVI and HIT-F specimens, the damage sites were protected, and the cores were cut from the carcass with a water knife. During the cutting process, the diameters were controlled to meet the parameters outlined in ASTM1499-C.

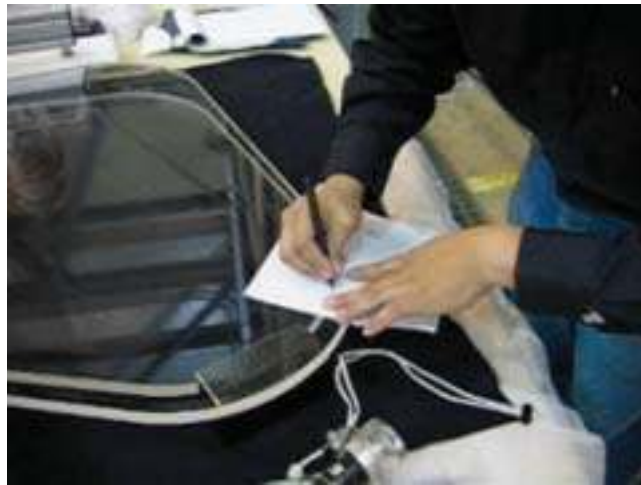


**Figure 6a.** Inflicting chatter check damage on a shuttle windowpane with a ball-point pen acting through a paper sheet on pane surface.

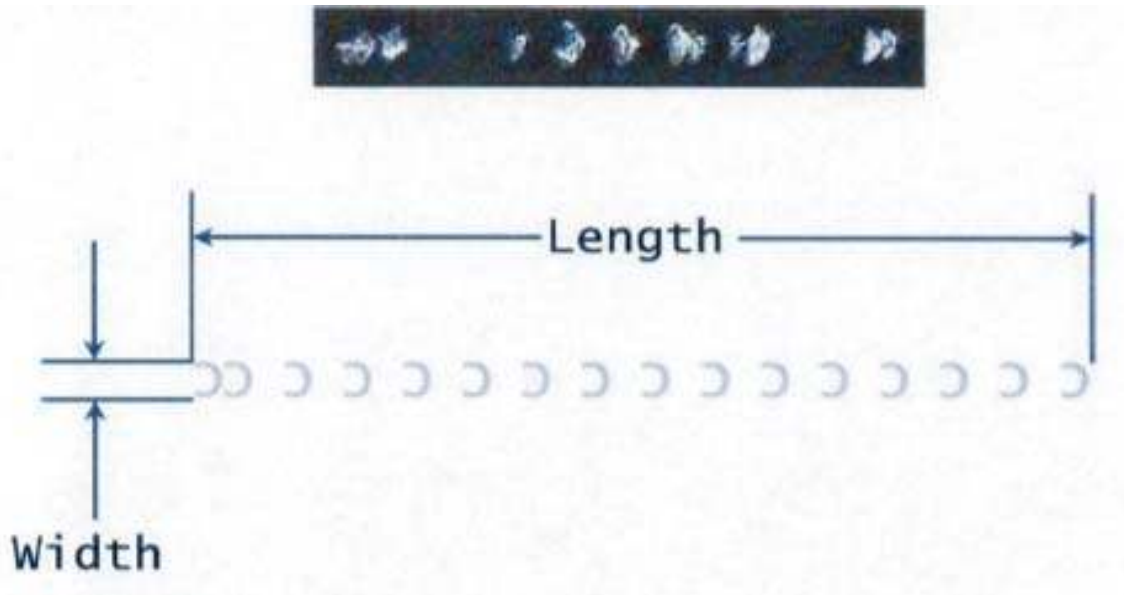


**Figure 6b**<sup>33</sup>. (Top) Photo showing chatter check damage inflicted in windowpane. (Bottom) Chatter Check measurement diagram.

Each damage site was measured using mold impressions and an optical micrometer, photographed, and imaged using the GFP device (Figure 7). The images were used to measure the *PER* amplitudes used in the stress analysis of regions surrounding the damage sites.

### III.A. Procedure with the GFP Device.

Circularly polarized light was used to form images of the damage sites, with the optical birefringence measurements from the GFP associated with each site being measured and recorded for each specimen. The birefringence measurements were converted into *PER* and averaged over a closed path that surrounds the damage site but far enough away to be in the elastic stress field around the damage site. This procedure was designed to specifically avoid optical discontinuities at the actual damage site. The resulting *PER* measured in this way and used in the analysis is proportional to the stress field at each damage site. The same technique was applied to all measured damage sites, regardless of classification. The same circumference was used for each set of measurements.

Geometrical measurements of the damage sites were also made with the GFP. The outer diameter of the damage site was determined by highlighting surface and internal damage by measuring loss of light intensity at the surfaces (internal and external). An analysis was made on a construct, which circumscribed the damage. The “diameter” of the construct was calculated by averaging a number of chord lengths across the construct, or by measuring the construct area,  $A_c$ , and determining the diameter by

$d = 2\sqrt{\frac{A}{\pi}}$ . The chatter-check dimensions were similarly determined. The shadow of the defect was filtered and a threshold was determined. The length was measured from tip to tip of the chatter check damage. The width was determined by the width of the shadow. The shadow was edge-detected, and dilated by 7 pixels to create an area mask for the stress calculation.



**Figure 7.** Engineer imaging and measuring *PER* at a damage site. A commercially available GFP with special software was used for these measurements.

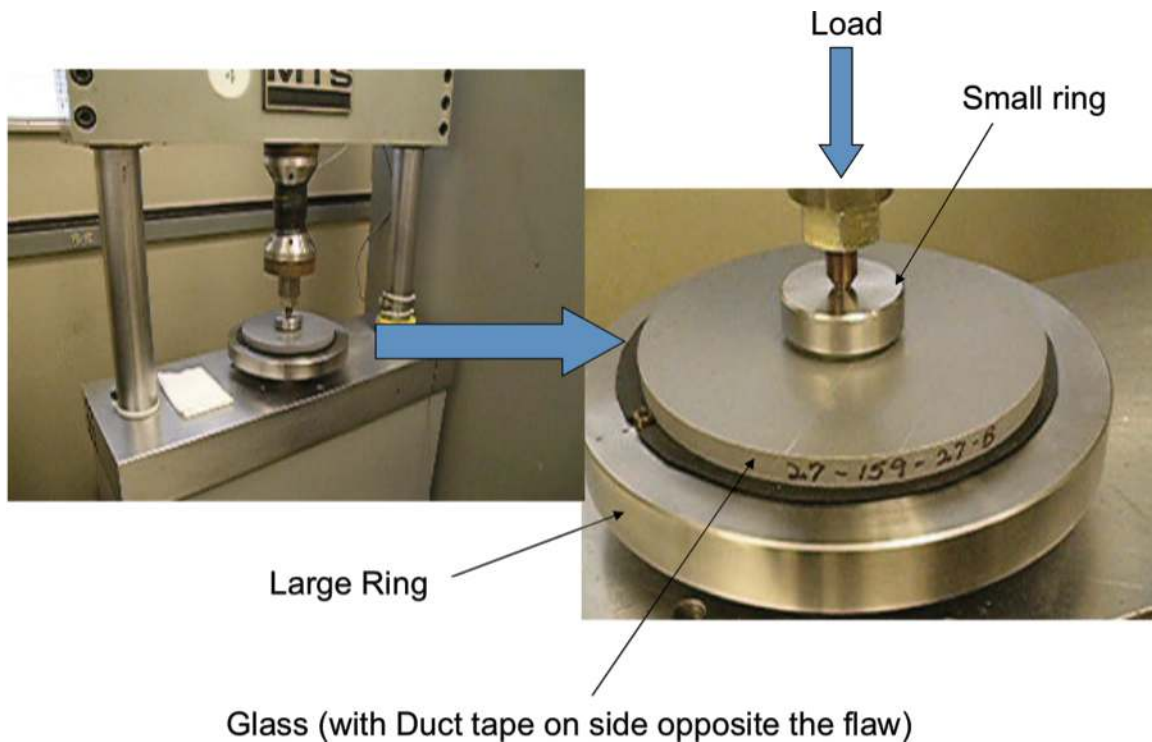


**Figure 8.** Ring-ring biaxial strength measurement of a specimen. In this figure the fracture strength of Specimen 27-159-27 (a Bruise specimen) is under measurement.

The fracture strength for each specimen was measured. Correlations were run between the fracture strength and the optical measurements including the results from the GFP.

### **IIIB. Results. The GFP Measurements.**

#### **1. HVI.**

Patterns from a typical hyper velocity impact (HVI) are shown in Figure 9. The analysis is shown graphically in Figure 10. In Figure 9, the image color shows the two states discussed in Eqs. (22) and (23). The color indicates the *PER* in nanometers associated with each stress state as labeled. The image shows the retardation in a color-coded format with the scale shown in the center. Further analysis of the image is shown

in Figure 10 (top), where the *PER* due to the total stress amplitude is shown as a function of  $r$ , the distance from the center of the damage site. One notices that the *PER* is largely radially symmetric with some structure that is azimuthally dependent. Within the image one also notices radially dependent structures of lower *PER* values that are formed. Beneath the image is a plot of the magnitude of the in-plane shear,  $\sigma_1 - \sigma_2$ , versus  $r$ . Based on the character of variations within the top image and the graph, one notices three zones in this diagram. In Zone 1, surrounding the impact site and extending out approximately 1.5 mm, we observe a center region where the *PER* is positive, followed by a region where *PER* is nearly zero. Within the near zero portion we see islands of large stress. Zone 2,  $[1.5 \text{ mm} < r < \sim 2.8 \text{ mm}]$ , is characterized by a mottled appearance, where we note concentric structures that appear to be separated by radial line segments, consistent with the generation of fields of edge dislocations where the extra planes are inserted radially outward from the impact site, and distributed throughout the damage zone. The appearance has a somewhat randomly appearing “clamshell” variation as indicated in the top of Figure 10. Zone 3,  $[r > 3 \text{ mm}]$  has a relatively smooth appearance and a gradual decrement in magnitude that extends out for a large distance from the center. Even in this region one observes substantial fluctuations. By using GFP technology, we observe that the measurable stress field extends far from the visible damage site.

## HVI Specimen 27-135-1

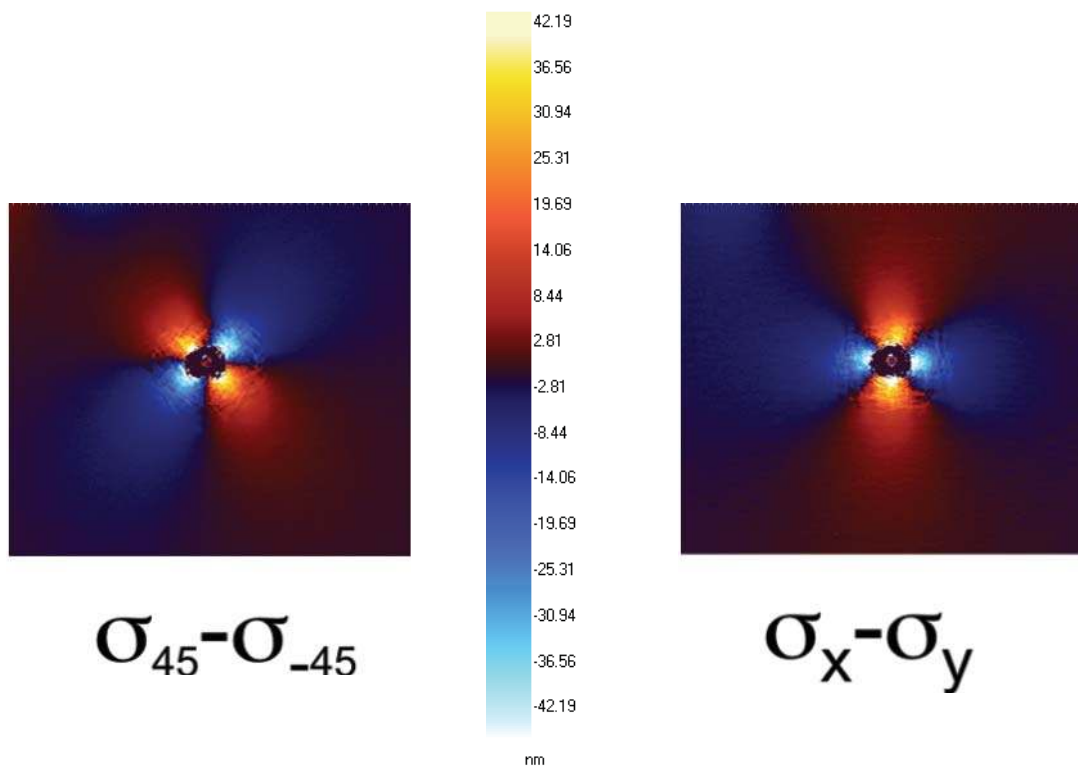


**Figure 9.** Stress-field image of the damage site from high velocity impact damage occurring in space, Specimen HVI 27-135. In the center of the color images is the photoelastic retardation –to-color scale in nanometers.



Beneath the graph is an optical image of a typical damage site taken in circularly polarized light. In this view a dark center appears, surrounded by less pronounced structures noted above. There is no view of the center structure that is so clearly evident in the *PER* image at the top. Close examination in the GFP image reveals a shadowy network with a grain boundary-like appearance near the prominent central feature. This indicates that patterns, within the plastic region, that become prominently visible in birefringence at and near the damage site.

### HVI Specimen 27-135-1 Maximum in-plane shear ( $\sigma_1 - \sigma_2$ )

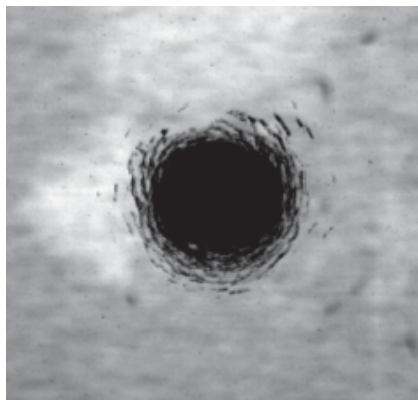
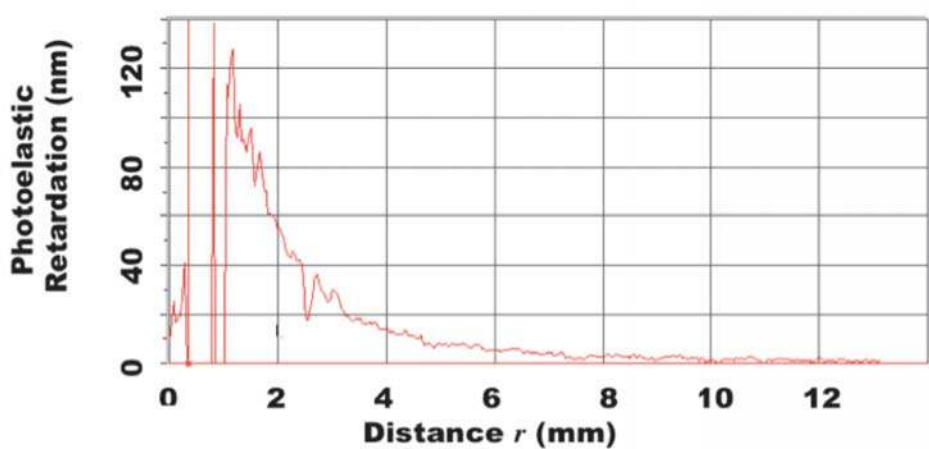
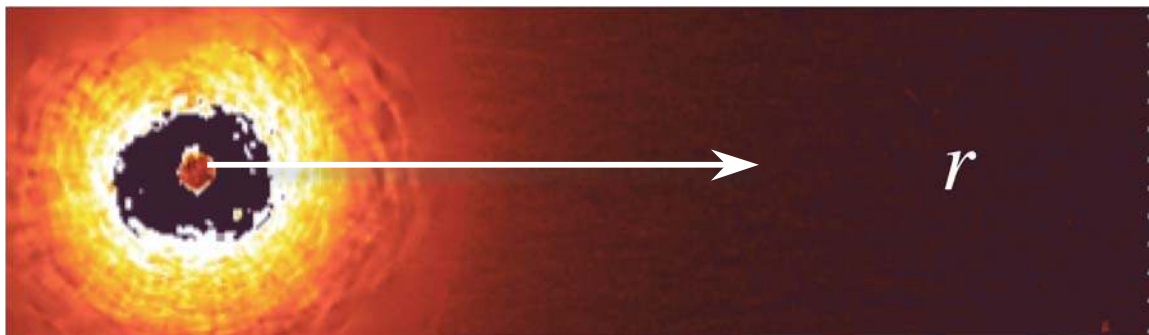


**Figure 10.** Photoelastic Retardation analysis for HVI Specimen 27-135-1 constructed from the data shown in Figure 9. Below graph is optical image of the damage site taken in circularly polarized light.

We analyze the HVI measurement results by least-squares fittings of the fracture strength (dependent variable) against 6 different independent variables. The results are given in Table 2. The dependent variable, fracture strength, is Y and the independent variable is x. The x-variables are given in the top row, and (in order) are the outer diameter and inner diameter of the damage site (as measured with the illumination from the circularly polarized light source from the grey-field polarizer), the *PER* measurement, the defect depth and defect depth to specimen thickness ratio, both measurements taken from the mold casting, and the defect size, taken from a measurement with an optical magnifier and scale. The equations used for the fits are shown in the extreme left column. The equation parameters are given for each fit.

$\begin{matrix} Y \\ \downarrow \\ \hline x \rightarrow \end{matrix}$	Outer Diameter (GFP)	Inner Diameter (GFP)	Photoelastic Retardation (GFP)	Defect Depth (Mold)	Depth to Thickness (Mold)	Defect Size (Optical)
$Bx+A$	A=45.8 B=-0.029 $R^2=0.532$	A=40.29 B=-0.076 $R^2=0.648$	A=39.5 B=-0.247 $R^2=0.805$	A=45.73 B=-35.2 $R^2=0.595$	A=45.61 B=-221.95 $R^2=0.588$	A=32.31 B=-0.513 $R^2=0.122$
$Ae^{Bx}$	A=47.2 B=-0.00086 $R^2=0.548$	A=40.44 B=-0.0023 $R^2=0.653$	A=39.3 B=-0.0075 $R^2=0.843$	A=47.04 B=-1.036 $R^2=0.609$	A=46.88 B=-6.526 $R^2=0.602$	A=32.00 B=-0.017 $R^2=0.112$
$A+B\log(x)$	A=106.0 B=-28.0 $R^2=0.581$	A=50.13 B=-9.545 $R^2=0.472$	A=43.1 B=-9.793 $R^2=0.991$	A=21.04 B=-24.53 $R^2=0.632$	A=1.505 B=-24.39 $R^2=0.627$	A=30.32 B=0.4039 $R^2=0.002$
$Ax^B$	A=274.2 B=-0.356 $R^2=0.593$	A=55.21 B=-0.13 $R^2=0.431$	A=43.7 B=-0.127 $R^2=0.997$	A=22.85 B=-0.310 $R^2=0.635$	A=12.94 B=-0.308 $R^2=0.631$	A=30.00 B=0.003 $R^2=0.002$

**Table 2.** Relationships between fracture strength of HVI-damaged specimens and six selected independent variables. Included are the fitting equation and the square of correlation coefficient ( $R^2$ ) for each fit.

The rankings of the correlation coefficients for each independent variable category in descending order of correlation are Photoelastic Retardation (GFP), Inner Diameter (GFP), Defect Depth (Mold), Defect depth to thickness ratio (Mold), Outer Diameter (GFP), and Defect Size (Optical). Within the equation types the power law best predicts the fracture strength except for the Defect Size (Optical), where the linear fit is slightly better. We suspect that this discrepancy is caused by the measurement uncertainty with the optical magnifier induced by variations of light paths caused by the optical disruptions at the damage site. The table shows that the best correlation occurs with a power-law fit of the fracture strength to the photoelastic retardation, thus affirming the results from theoretical predictions.

We further analyze the power-law fit between the Fracture Strength and *PER*. In Figure 11 we calculate the least squares power-law fit and obtain a square of the correlation coefficient R. As predicted by the theory, this is the best fit with a correlation coefficient of 0.998 ( $R^2=0.9967$ ). Thus the theoretical analysis for the relationship between fracture strength and *PER* is confirmed for HVI damage.



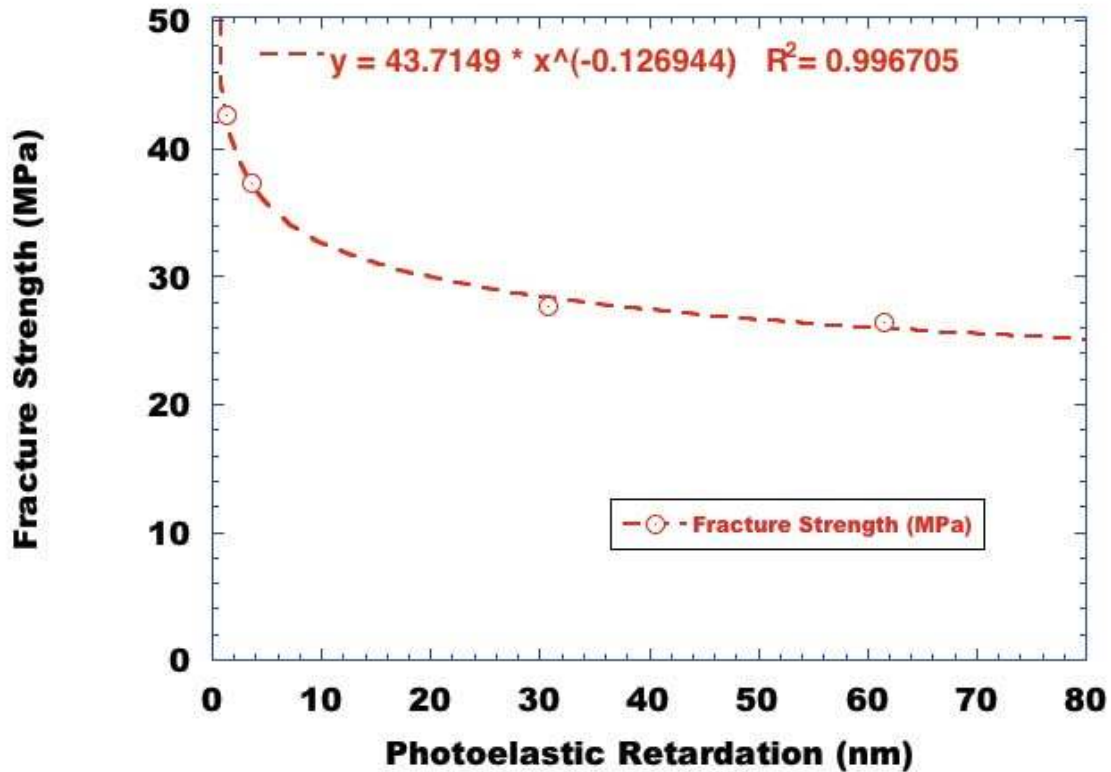


**Figure 11.** A plot of measured fracture strength versus photoelastic retardation for hyper velocity impacts .

## 2. Bruises.

In Figure 12, we have images from a typical measurement obtained from a bruised specimen. The figure shows the stress image of a bruised specimen (left) and an optical image (right) taken with circularly polarized light. The stress image also shows relatively low values of stress-induced birefringence (SIB) in the central zone. Outside the center zone we find regions of low SIB in the positive (red in color) regions , and regions of much higher SIB (white) in both the positive and negative regions. Separation zones between positive and negative stresses are curled, where in the HVI, the separations were straight. Many of the same prominences appear in the optical image (circularly polarized illumination) of the bruise as well, but are less pronounced. In both images the center is slightly affected, with a positive SIB showing in the *PER* image. Most of the damage appears around the perimeter of the center zone. A slight SIB variation in the central feature appears across the central zone. Just beyond the central zone regions (corresponding to Zone 2 in the HVI), the SIB shows some features that stand out from the background. These features fall into two different shape classifications. Some features follow a circular or radially symmetric appearance. Other features appear to have a dependency that has a spiral or involuted appearance. Both features show that the strain pattern has regions with prominences, indicating substantial localized strains. But in comparison to the typical HVI pattern, the *PER* range is similar.

The damage site was also measured with an optical micrometer with the aid of a Surface Light Optimization Tool (SLOT), which directs high intensity light into the plane of the glass, at the damage site. These data were used in compiling the comparisons in Table 3.

## Bruise 27-139-15

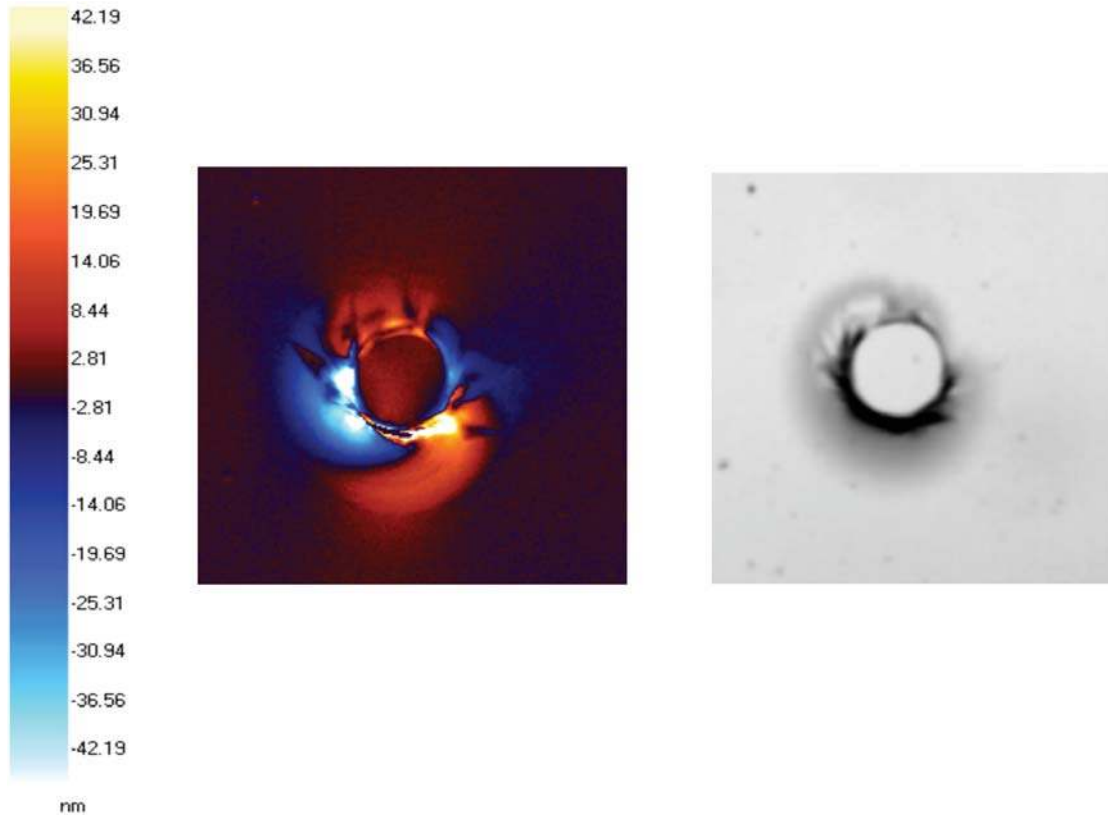


**Figure 12.** Stress Field Image (left) and visual image under circularly polarized light (right) of a typical bruised specimen. At the left of the color image is the photoelastic retardation –to-color scale in nanometers.

Table 3 gives the least-squares fit of the fracture strength (dependent variable) of a set of specimens, each with a bruise damage site, to different measurements taken for the independent variable. Correlation coefficients are relatively high for the Outer Diameter measured with circularly polarized light illumination from the GFP and the Photoelastic Retardation measurement. Additionally for these two independent variable choices the power law is the best fit. The highest correlation coefficient,  $R=0.990$  ( $R^2=0.981$ ) occurs between the Fracture Strength and the *PER* measured with the GFP. A closer examination of the fit is shown in Figure 13, which is a plot of the fracture strength versus the Photoelastic Retardation for the bruise specimens.

### 3. *HIT-F*

This class of damage is inflicted with hyper velocity projectiles of varying materials, sizes and shapes and at various angles (See Table 1 for the details). The velocity at impact can be varied and measured precisely, so that projectile energy is known. The typical resulting damage site is shown in Figure 14, which shows the stress-induced birefringence image (left) and an image taken with circularly polarized light (right). There is substantial clamshell cracking, called conchoidal spall, that a substantial distance from the impact site. The site appears to have a bright center surrounded by a

Y ↓ x→	Outer Diameter (GFP)	Inner Diameter (GFP)	Photoelastic Retardation (GFP)	Ave. Outer Diameter. (Slot+Edge)	Ave. Inner Diameter. (Slot+Edge)
$Bx+A$	A=50.09 B=-0.0658 $R^2=0.679$	A=59.53 B=-0.305 $R^2=0.333$	A=37.26 B=-1.199 $R^2=0.625$	A=48.16 B=-137.4 $R^2=0.651$	A=53.17 B=-639.6 $R^2=0.311$
$Ae^{Bx}$	A=58.54 B=-0.00247 $R^2=0.794$	A=93.96 B=-0.012 $R^2=0.304$	A=36.32 B=-0.0455 $R^2=0.735$	A=54.66 B=-5.19 $R^2=0.748$	A=72.96 B=-26.37 $R^2=0.272$
$A+B\log(x)$	A=177.45 B=-59.859 $R^2=0.816$	A=182.9 B=-77.20 $R^2=0.312$	A=39.42 B=-19.11 $R^2=0.973$	A=-19.44 B=-54.70 $R^2=0.775$	A=-58.01 B=-60.67 $R^2=0.274$
$Ax^B$	A=5686.8 B=-0.941 $R^2=0.913$	A=14946 B=-1.38 $R^2=0.273$	A=37.16 B=-0.282 $R^2=0.981$	A=4.513 B=-0.866 $R^2=0.861$	A=0.7362 B=-1.09 $R^2=0.221$

**Table 3.** Relationships between fracture strength of bruised specimens and selected independent variables. Included with the equation for each fit is the square of correlation coefficient ( $R^2$ ) for the fit.

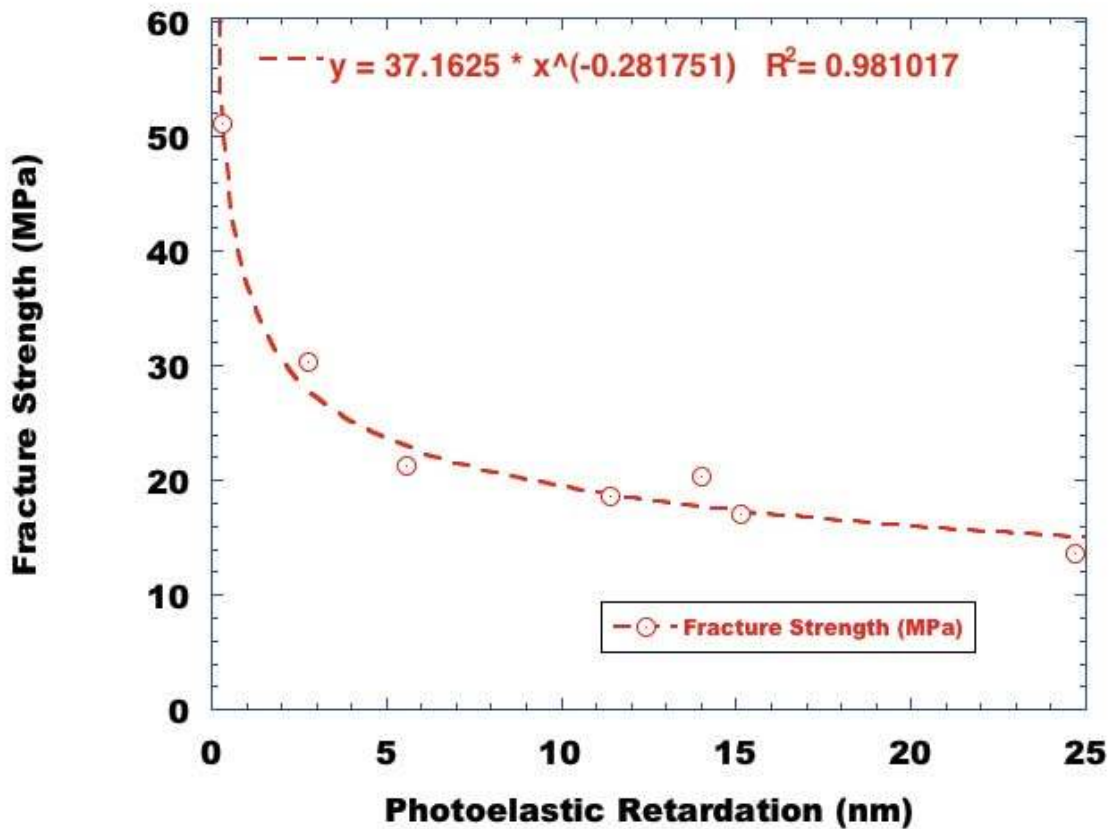


**Figure 13.** A plot of fracture strength versus photoelastic retardation for bruise damage in glass.

dark central region. Directly beyond this is a region where concentric bands appear and extend beyond what appears as impact-related patterns in the glass. This is prominent in both images, as are a series of radial patterns emanating from the impact center. This appears in both the SIB image and the image formed by circularly polarized light. As in the other images, the strain field extends far from the impact site. In this case, however, more structure also appears in the image taken with circularly polarized light. In both images (SIB and circularly polarized light) sharp variations in radial directions appear.

## HITF 05305

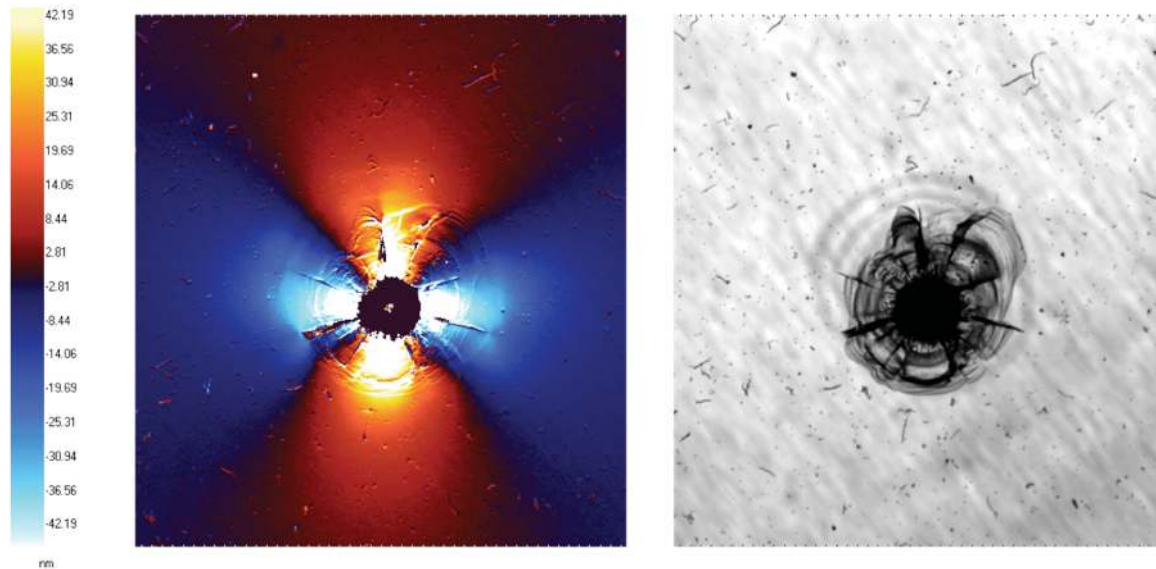


**Figure 14.** Stress induced birefringence image (left) and visual (right) of a typical impacted site. At the left of the color image is the photoelastic retardation –to-color scale in nanometers.

We analyze the five specimens, which were used in this study. Only three specimens had *PER* data. Even though the data is statistically insignificant, we include the HIT-F data for completeness. The HIT-F measurements are evaluated by forming a least-squares fits of the fracture strength (dependent variable) against 6 different independent variables. The results are given in Table 4. As before, the dependent variable, fracture strength, is  $Y$  and the independent variable is  $x$ . The  $x$ -variables are (in order) the outer diameter and inner diameter of the damage site (as measured with the illumination from the circularly polarized light source from the grey-field polarizer), the *PER* measurement, the defect depth taken from the mold casting, and the defect size, taken from a measurement with an optical magnifier and scale. Each set is analyzed for best-fit correlation, with the equation parameters given for each fit. The equations used for the fits are shown in the extreme left column. The top row gives the independent variable used for the fit.

The rankings of the correlation coefficients for each independent variable category (best to worst) are Inner Diameter (GFP), Defect Size (Optical), Outer Diameter (GFP), Defect Depth (Mold), Defect to thickness (Mold), and Photoelastic Retardation (GFP). The exponential and log fits appear to be the best of the equation forms evaluated against the fracture strength. The power law is not the best except for the *PER*. Although

not the best match, the inner diameter has a good correlation coefficient of  $R=0.977$  ( $R^2=0.955$ ) shown in Figure 15. We are unable to draw conclusions because of the paucity of data, especially for the Photoelastic Retardation measurements (3 points), since only three of the specimens were able to render a *PER* reading because surface spalling caused excessive light path scattering. However, a graph of fracture strength vs. *PER* is included, (Figure 16) even though the least squares fit (and hence its Correlation Coefficient) is not sufficiently representative of the process to be able to draw conclusions.

$\begin{matrix} x \rightarrow \\ Y \\ \downarrow \end{matrix}$	Outer Diameter (GFP)	Inner Diameter (GFP)	Photoelastic Retardation (GFP)*	Defect Depth (Mold)	Defect Length/Dia. (Mold)	Defect Size (Optical)
$Bx+A$	A=41.36 B=-0.0068 $R^2=0.860$	A=41.39 B=-0.035 $R^2=0.882$	A=41.70 B=-0.374 $R^2=0.234$	A=40.95 B=-12.29 $R^2=0.876$	A=47.24 B=-211.85 $R^2=0.841$	A=42.44 B=-0.957 $R^2=0.901$
$Ae^{Bx}$	A=42.47 B=-0.00025 $R^2=0.846$	A=43.00 B=-0.0013 $R^2=0.917$	A=41.27 B=-0.0089 $R^2=0.243$	A=41.93 B=-0.450 $R^2=0.865$	A=52.05 B=-7.56 $R^2=0.798$	A=44.35 B=-0.035 $R^2=0.902$
$A+B\log(x)$	A=81.00 B=-17.175 $R^2=0.865$	A=82.29 B=-22.74 $R^2=0.967$	A=44.77 B=-8.409 $R^2=0.487$	A=24.72 B=-14.60 $R^2=0.865$	A=2.172 B=-23.74 $R^2=0.743$	A=49.44 B=21.03 $R^2=0.905$
$Ax^B$	A=166.2 B=-0.259 $R^2=0.856$	A=180.99 B=-0.351 $R^2=0.955$	A=44.52 B=-0.0887 $R^2=0.516$	A=23.53 B=-0.218 $R^2=0.836$	A=11.12 B=-0.346 $R^2=0.691$	A=55.55 B=0.319 $R^2=0.875$

**Table 4.** Relationships between fracture strength of HIT-F-damaged specimens and selected independent variables. Included with the equation for each fit is the square of Correlation Coefficient ( $R^2$ ) for the fit. Three points were used for the determination of fits to the Photoelastic Retardation, and is indicated by \*.

We further note that the accuracy of optical measurements with this damage are less because light is badly scattered by the crazing that extends from the center to a good distance from the damage site. Depending on surface disruptions, significant portions of the light beam may be scattered from the site.

#### 4. Chatter Checks

This class of damage is inflicted with dull object pulled across the surface of the glass. Other than the force necessary to hold the object to the surface, no particular normal force is applied to the dull object as it scrapes across the glass surface. The typical resulting damage site is shown in Figure 17, which shows the stress-induced birefringence image. The site appears to have a bright centerline with indications of strain patterns extending, somewhat randomly, normal to the line. In contrast to the other images, the strain fields do not extend far from the scratch (damage site).



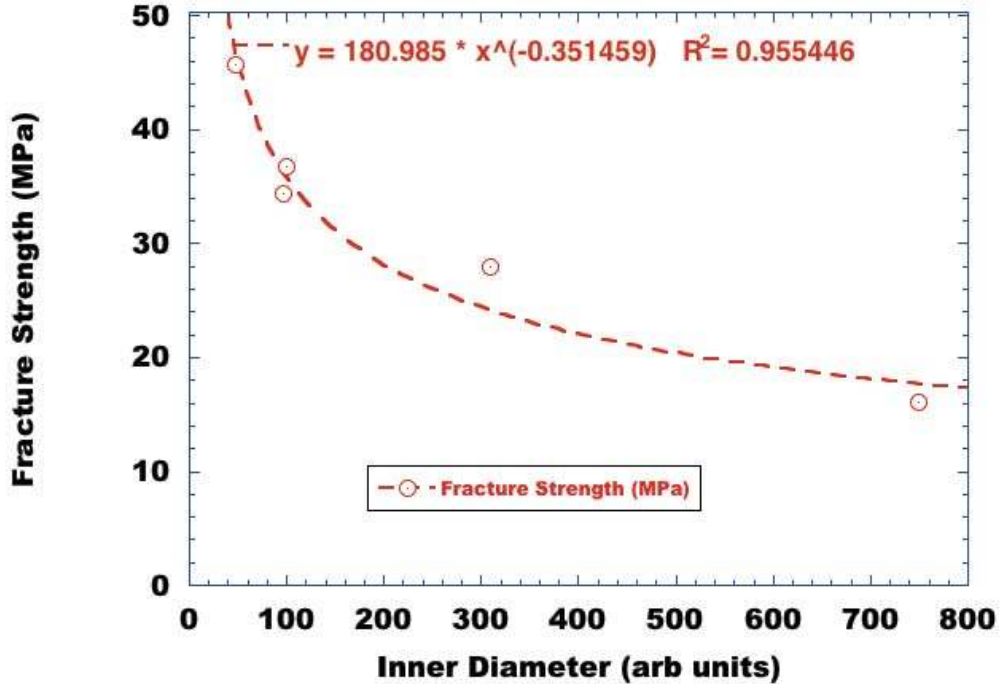


**Figure 15.** A plot of fracture strength as a function of GFP measurement of damage site inner diameter in HIT-F-damaged specimens.

We analyze twelve specimens that were used in this study. The Chatter Check measurement results are analyzed by forming least-squares fits of the fracture strength (dependent variable) against 5 different independent variables. The results are given in Table 5. As in the earlier classifications, the dependent variable, fracture strength, is Y and the independent variable is x. The x-variables are (in order) the outer length (GFP measurement), outer breadth (GFP measurement) of the damage site (as measured with the illumination from the circularly polarized light source from the GFP), the *PER* measurement, the outer length from an optical micrometer aided by the SLOT. Each set is analyzed for best-fit correlation, with the equation parameters given for each fit. As before, the equations used for the fits are shown in the extreme left column. The top row gives the independent variable used for the fit.

The rankings of the correlation coefficients for each independent variable category (best to worst) are Outer Length from SLOT Measurement, Outer Length (GFP), Area from Slot Measurement, Photoelastic Retardation (GFP), and Outer Breadth (GFP). The power law equation form best predicts the fracture strength (has the higher correlation coefficient), except for outer breadth, where the linear form is the best fit. Whether measured with the GFP or the SLOT measuring instrument, the outer length appears to be the best predictor, with a correlation coefficient of 0.578 ( $R^2=0.335$ ). Generally, the low correlation parameters suggest that none of these variable are predictive of the fracture strength. It is instructive to examine a graph of fracture strength vs. *PER* (Figure 18) even though the least squares fit (and hence its correlation coefficient) is not the best in the list. We find that most of the scatter appears with specimens where the *PER* is less than 1 nm. For comparison fracture strength plotted against outer length is shown in Figure 19. Unfortunately, most of these data lies in the range where *PER* is less than 1 nm.

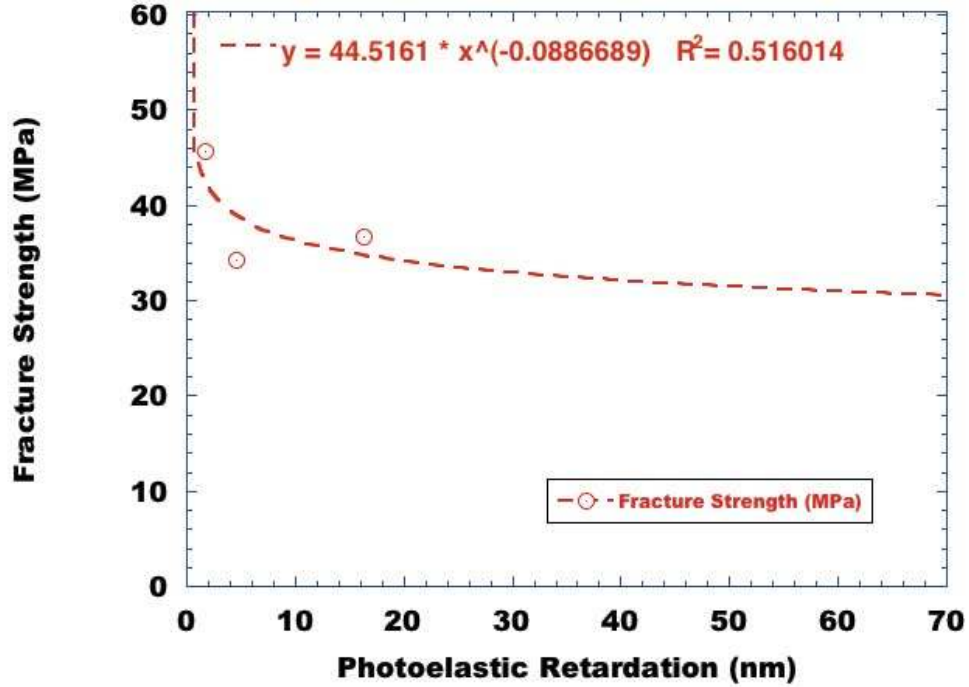


**Figure 16.** A plot of fracture strength of HIT-F-damaged specimens as a function of photoelastic retardation. Only 3 points available make plot inconclusive.

$\begin{matrix} x \rightarrow \\ Y \downarrow \end{matrix}$	Outer Length (GFP)	Outer Breadth (GFP)	Photoelastic Retardation	Outer Length from Slot Measurement	Damage Area from Slot Measurement*
$Bx+A$	A=70.617 B=-0.117 $R^2=0.205$	A=76.85 B=-0.827 $R^2=0.109$	A=69.404 B=-8.558 $R^2=0.147$	A=70.31 B=-26.702 $R^2=0.184$	A=69.98 B=-5.17 $R^2=0.159$
$Ae^{Bx}$	A=70.43 B= $-1.77 \times 10^{-4}$ $R^2=0.212$	A=77.56 B=-0.013 $R^2=0.108$	A=69.208 B=-0.132 $R^2=0.149$	A=70.07 B=-0.403 $R^2=0.192$	A=69.73 B=-0.0782 $R^2=0.167$
$A+B \log(x)$	A=104.74 B=-15.173 $R^2=0.321$	A=94.60 B=-25.76 $R^2=0.099$	A=60.072 B=-14.66 $R^2=0.167$	A=53.69 B=-14.793 $R^2=0.321$	A=63.9 B=-14.96 $R^2=0.306$
$Ax^B$	A=117.22 B=-0.0986 $R^2=0.334$	A=102.15 B=-0.173 $R^2=0.097$	A=59.89 B=-0.099 $R^2=0.167$	A=54.65 B=-0.096 $R^2=0.335$	A=63.58 B=-0.0971 $R^2=0.322$

**Table 5.** Relationships between fracture strength of specimens with chatter-check damage sites and selected independent variables. Included with the equation for each fit is the square of correlation coefficient ( $R^2$ ) for the fit. \* indicates a calculated value (length x width\*1000 ; arb. Units . See Fig. 6b for detail used to calculate area)



# Chatter Check Specimen 26-210-30

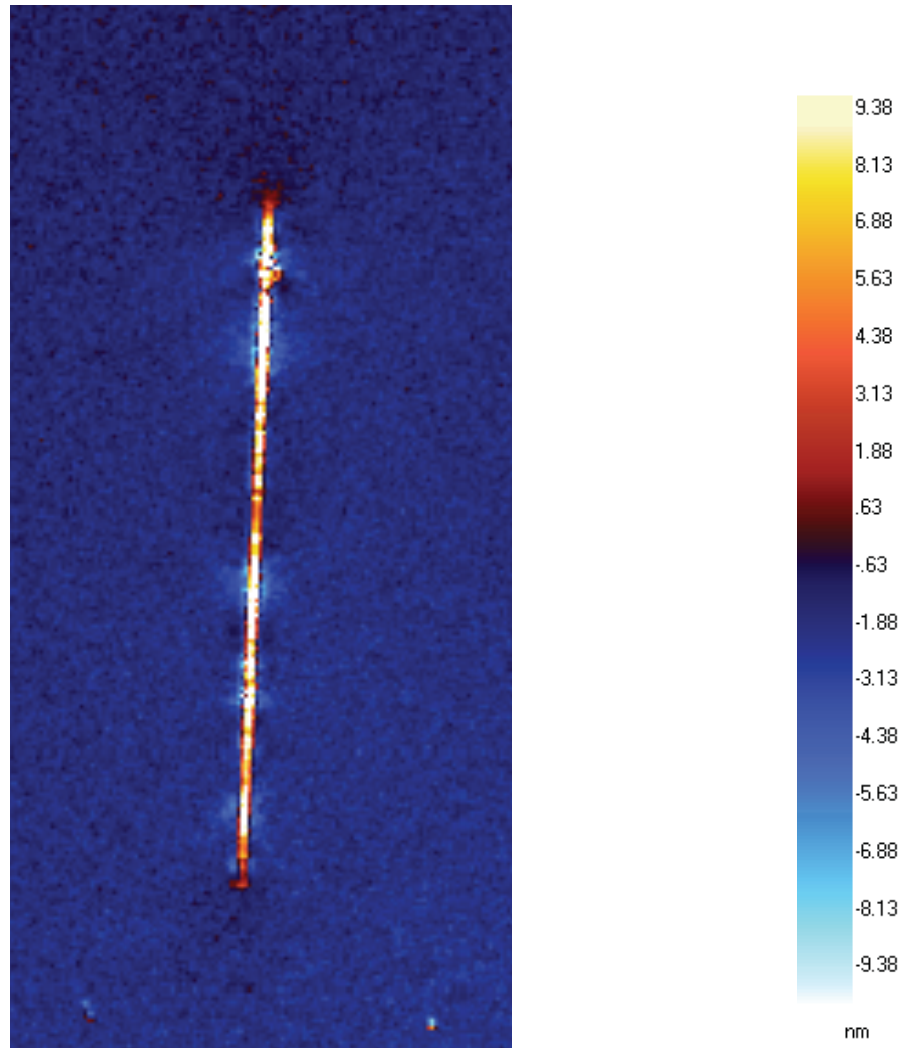


**Figure 17.** Stress-field image of Chatter Check, showing effects of stress fields around the damage (line). To the right of the image is the *PER* color scale in nanometers.

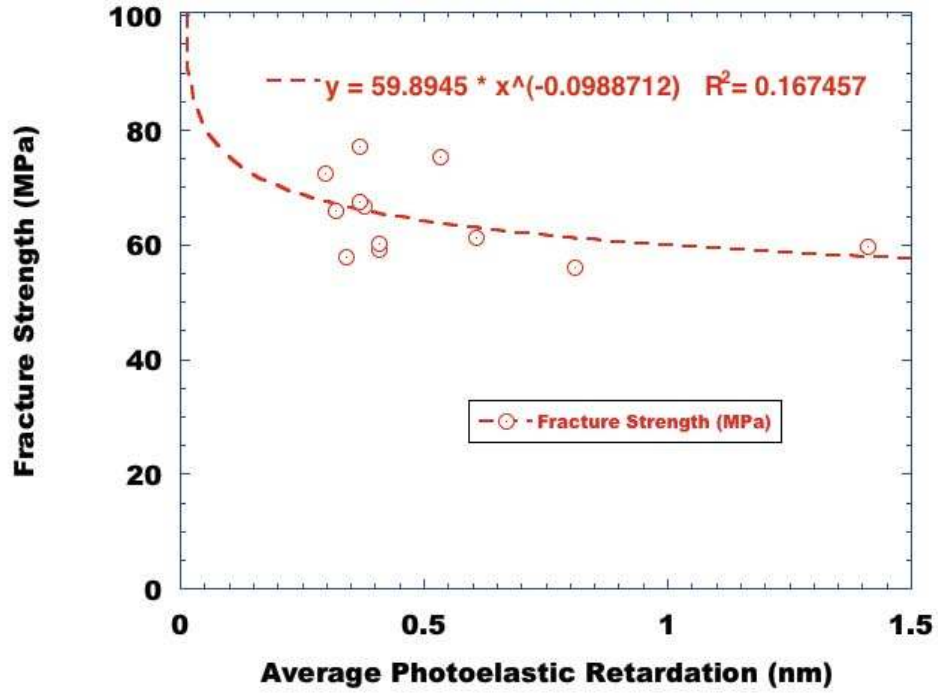


Figure 18. A plot of fracture strength versus average photoelastic retardation for Chatter Checks.

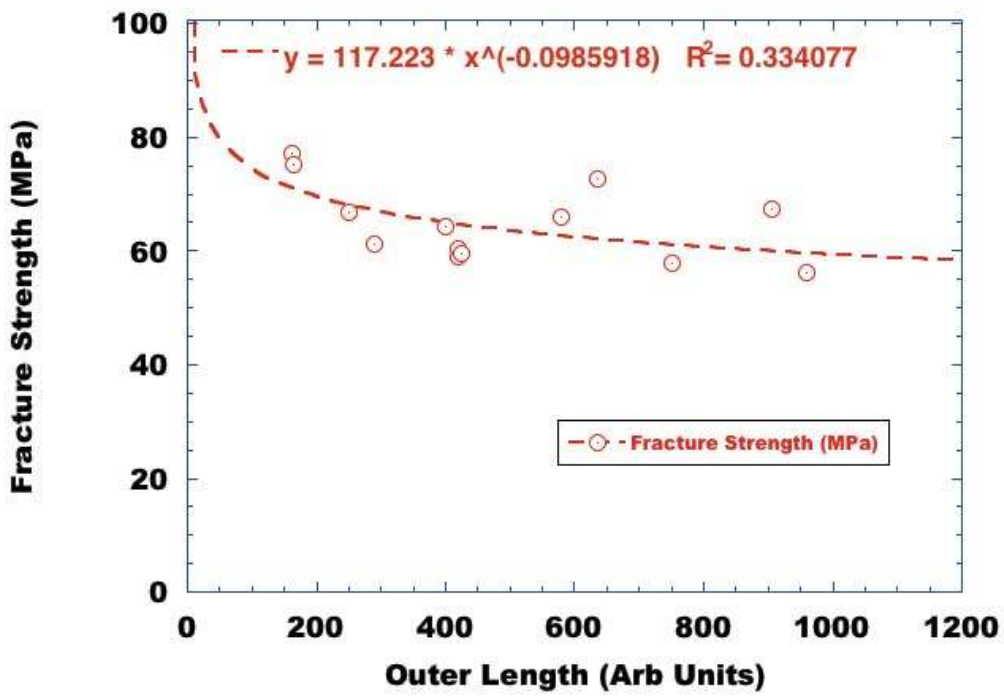


Figure 19. A plot of fracture strength versus outer length for chatter checks.

## IV. DISCUSSION

We began this project to improve the location and detection of damage sites as an aid to technicians who examined each window on returning shuttles for damage. As the data were collected we observed that *PER* measurements were predictive. At this point we developed an analytical model to relate fracture strength of fused silica to *PER* measurements. Furthermore, we checked the fracture strength of a somewhat randomly selected (within each category) sampling of specimens against their *PER* measurements. We used the somewhat random selection of the data to establish parameters against which the remaining data can be compared. The results of this comparison will be the basis of a later study. The random selection of the data was chosen for this work so that an estimate of uncertainty can be made. The uncertainties are estimated by comparing values calculated from the least-squares power fits with the measured data against the *PER* measurements. Table 6 gives the results of the estimates of uncertainty of *PER* measurements for each damage classification.

Damage Classification	HVI	Bruise	HIT-F	Chatter Check
Uncertainty (MPa)	±0.8	±1.8	±4.2	±6.5

**Table 6.** Uncertainties for calculations from least-squares fits of the fracture strength to the photoelastic retardation for each damage type.

Table 7 (below) gives the constants associated with the least-squares data analysis for fracture strength versus *PER*. In the first two rows the constants are given for the power law ( $y=Ax^b$ ) fit, determined by theory to be the best functional form for relating fracture strength to damage.

Damage Type → Constants ↓	HVI	Bruise	HIT-F	Chatter Check
$A$	43.71	37.16	44.52	59.89
$B$	-0.127	-0.2817	-0.0887	-.0099
$\zeta$	5.25	2.37	7.52	6.73
$\chi$	43.71	37.16	44.52	59.89

**Table 7.** A Summary of constants associated with the different damage classifications in this study.  $\chi$  is equal to  $A$  and is repeated here for emphasis.

For each of the damage types listed, the constant  $\chi$  ( $= A$  in Equation 36) is the value of the fracture strength (in MPa) for one nm of photoelastic retardation.  $\chi$  shows a very small difference for the hyper-velocity impacts (HVI and HIT-F damage), while showing substantially more difference for the bruises and chatter checks. The origin of this variation is suspected to be differences in the constant factors (shape factors and other geometrically-related constants, photo-elastic constants, energy threshold effects and load rates) that contribute to  $\chi$ . Based on the present data, Eqs. (14b), and (36),

particle shape has little effect on  $\chi$  for high velocity regimes, since the hyper velocity impacts (HVI) and impacts from the Hypervelocity Impact Technology Facility (HIT-F) appear to nearly match in value of  $\chi$ . However within the same regime, impactor characteristics such as shape and composition appear to affect the dynamics of the conversion process within the glass, as seen with the variation in  $\zeta$  for HVI and HIT-F inflicted damage. The constant  $\zeta$  shows a variation in effective lengths of plastic strain regions. This is not surprising since a large number of possible paths are available for the conversion process within the glass from differing indenter shapes and properties (density, hardness, etc.).

Damage Type → Minimum <i>PER</i> ↓	HVI	Bruise	HIT-F	Chatter Check
$I_{min} (nm)$	0.456	0.323	0.399	8.81

**Table 8.** Minimum *PER* for each of the Damage Classifications for a fracture strength equal to the published tensile strength for fused silica.

It is instructive to determine the values of *PER* for each classification at which the fracture strength is no more than the published tensile strength of 48.3 MPa<sup>34</sup>, for fused silica. Table 8 shows the values for each type of damage classification analyzed here. We also note that an examination of Chatter Check Damage (Figure 18) shows an interesting feature about the relationship between strength and the degradation threshold for *PER*. The fracture strength appears random for values of *PER* below ~0.6 nm, indicating a possible minimum damage below which the fracture strength is not affected. Thresholds for degradation for chatter checks indicate that *PER* sensitivity is adequate for a nondestructive methodology to inspect windows for aerospace usage for this classification of damage. It therefore is an area for further investigation to determine a minimum *PER* in each classification below which impact damage does not exceed the effects of inherent flaws in the glass on strength.

HIT-F inflicted damage analysis shows that *PER* is unable to give measurements if the physical disruption of the surface leads to excessive light scatter. Unless one develops a technique to avoid the surface scattering at the damage site, another technique would need to be employed for analysis of such damage. Our data suggest that the inner diameter of the damage site gives best predictive results for this type of damage. In this case, the inner diameter measured with the GFP system gave the most reliable predictions. The optically-measured defect size and the defect depth (mold) also gave good results.

Bruise damage shows a center where *PER* is largely unaffected. Most of the large variation in birefringence occurs at the perimeter of the physical damage site. Measurements other than *PER*, but made with the GFP optical instrument also show promise for bruise damage assessment as well. The GFP optical image measurements of outer diameter damage of bruises are a good predictor of fracture strength.

The depth measurement using molds (HVI) appear to provide the next most reliable indications of fracture strength in glass. Chatter Checks do not show the same reliability of prediction in any of the measurement techniques that were tested. But of all measurements on Chatter Checks, the outer length appears to be the most predictive. Part

of the reason for this is that the effect of chatter checks on the fracture strength was much less than the other modes of damage, and the size of each craze-site along the length was uniform.

We again point out that the theory developed for the relationship between PER and fracture strength depends upon the theory for collision kinetic energies and fracture strength, which is based on a quasi-static analysis, and hence is limited. Since this analysis is applied to a very dynamic situation, the framework is missing rate-related elements. While it allows for different collision classifications, it doesn't analytically treat the different pathways by which energy is imparted by the particle to the glass. None-the-less, its predictive power is quite good, as is its ability to assist in the development of solid and reliable experimental procedures. It predicts the power-law dependence, which is consistent with current damage models for glass. This quasi-static analysis introduces a damage response mechanism of dislocation formations within the glass in response to damage-causing impacts. Furthermore this work points to a basis for a systematic treatment of damage analysis and fracture strength prediction from grey field polariscope-based measurements in annealed fused silica.

## V. CONCLUSIONS

Measurements on shuttle windows were taken to determine the geometrical and the birefringence characteristics of different types of inflicted damage with various optical devices. Measurements of each site were taken with a variety of techniques, including the use of various magnifiers for geometrical optical image analysis that included direct measurements and measurements on molds made of damage sites. A commercially available grey-field polariscope was also used to measure simultaneously an image of the damage site and the photoelastic retardations at each damage site. After these measurements were made, each specimen was broken in accordance to ASTM Standard C1499-09. The fracture strength for each specimen was curve-fitted to four standard functions by using least-square fitting routines, and the correlation coefficients were compared. Consistent with the theory relating fracture strength to photoelastic retardation measurements as prescribed, the power law fit gives the best results for Hyper Velocity Impact damage and bruise damage. Chatter check damage correlation with fracture strength was best predicted by damage length because a well-defined crack length is formed. HIT-F-inflicted damage correlated best with inner diameter measurements of the damage sites.

The results show that, as predicted by theory, the power-law correlation between the GFP measurements and fracture strengths  $\sigma_f$  gives the best fit, with the results as follows:

$$\sigma_f = 43.7 (\epsilon)^{-0.127} \quad R^2 = 0.997 \quad (\text{HVI-photoelastic retardation})$$

$$\sigma_f = 181.0 (\epsilon)^{-0.351} \quad R^2 = 0.955 \quad (\text{HIT-F-inner diameter damage})$$

$$\sigma_f = 37.2 (\epsilon)^{-0.282} \quad R^2 = 0.981 \quad (\text{Bruises-photoelastic retardation})$$

$$\sigma_f = 117.2 (\epsilon)^{-0.099} \quad R^2 = 0.334 \quad (\text{Chatter Checks-outer length of scratch})$$

where  $\epsilon$  is the corresponding damage parameter (e.g. photoelastic retardation) measurement. Both the theoretical and experimental components of this study clearly establish the fact that photoelastic retardation is a valid technique to assess fracture strength degradation of annealed fused silica from high velocity impacts encountered during flight. This study further outlines the framework of an experimental analysis for a photoelastic retardation-based method to accomplish this. This study also affords a comparison of the effectiveness of different evaluation techniques to assess effects of

impact damage on the service life of fused silica windows. We conclude that the optical birefringence assessment of damage sites is a good indicator of fracture strength in annealed fused silica and hence a good inspection technique for aiding in the determination of retirement-for-cause for annealed fused silica windows used for space applications. This conclusion is based on correlations among different measurements with the fracture strength measured in specimens prepared from shuttle windowpanes.

## VI. ACKNOWLEDGEMENTS

The authors wish to acknowledge and thank the following, who helped with this work. Brad Boyce (Stress Photonics) wrote much of the data collection software used with the GFP system. Marshall Neipert (NASA/JSC), systematically created the bruises and chatter checks that were used in this study. Ray Parker (NASA/LaRC) took the x-ray tomographic data on a damage site in silica. Karen Bernstein (NASA/JSC) held up a significant portion of her study so that we could collect the GFP data on the HVI and HIT-F damaged specimens. We also wish to thank Richard W. Russell (NASA/KSC) for funding the Stress Photonics portion of the data collection.

## VII. REFERENCES AND NOTES

- <sup>1</sup> In the past, these panes have been manufactured from Corning 7940/7989 Fused Silica glass.
- <sup>2</sup> S. M. Wiederhorn and B. R. Lawn, "Strength Degradation of Glass Impacted with Sharp Particles: I, Annealed Surfaces", *J. Am. Ceram. Soc.*, **62**, pp. 66-70, (1979).
- <sup>3</sup> B. R. Lawn, D. B. Marshall, and S. M. Wiederhorn, "Strength Degradation of Glass Impacted with Sharp Particles: II, Tempered Surfaces", *J. Am. Ceram. Soc.*, **62**, pp. 71-74, (1979).
- <sup>4</sup> Edelstein, Karen S. "Orbital impacts and the Space Shuttle windshield", NASA-TM-110594, NASA. Johnson Space Center, 1995.
- <sup>5</sup> For example of an analysis, see S. M. Wiederhorn, A. G. Evans, E. R. Fuller, and H. Johnson, "Application of Fracture Mechanics to Space-Shuttle Windows", *J. Am. Ceram. Soc.*, **57**, pp. 319-323, (1974).
- <sup>6</sup> B. A. Proctor, I. Whitney, and J. W. Johnson, "The strength of fused silica", *Proceedings of the Royal Society of London, Series A, Mathematical and Physical Sciences*, **297**, pp. 534-557, (1967).
- <sup>7</sup> An example of this is Richard R. Burt, and Eric L. Christiansen, "Hypervelocity Impact Testing of Transparent Spacecraft Materials", *Intl. J. Impact Engineering*, **29**, pp. 153-166, (2003).
- <sup>8</sup> Max Born and Emil Wolf, "Principles of Optics", 4<sup>th</sup> Edition, Pergamon Press, Oxford, UK, pp. 703-718, (1970).
- <sup>9</sup> An orbiter window inspection system was designed and built by ASRC (Arctic Slope Resource Corp.) and NASA Kennedy Space Center. This design used a modified GFP unit based largely on the Stress Photonics GFP-2400 commercially modified, built, and tested by Stress Photonics.
- <sup>10</sup> The damage classifications were developed to cover the range of damage infliction to the window. All but the naturally occurring High Velocity Impacts (HVI) are idealized.
- <sup>11</sup> "Standard Test Method for Monotonic Equibiaxial Flexural Strength of Advanced Ceramics at Ambient Temperatures", ASTM Standard C1499-09, ASTM International, Conshohocken, PA (2009).
- <sup>12</sup> This assumption is restrictive because damage caused by different speeds of particles has different energy dependencies. In this case we use a quasi-static approach, which limits its applicability. However, the power-law dependency on energy appears to be broadly applicable, even though the power-law parameters change under the differing initial conditions (velocity, particle diameter, etc).
- <sup>13</sup> Estes, Lynda R., "Strength Design and Verification Criteria for Glass, Ceramics, and Windows



in Human Space Flight Applications”, NASA Technical Standard, NASA-STD-5018, Oct, 2010. Also See Reference 2.

<sup>14</sup> There are various energy-loss mechanisms. The list includes sound-wave generation, modal vibrations and heat generation.

<sup>15</sup> B. R. Lawn and D. B. Marshall: pp. 205-229 in Fracture Mechanics of Ceramics, Vol. 3, edited by R. C. Bradt, D. P. H. Hasselman, and F. F. Lange, Plenum, New York, (1978).

<sup>16</sup> B. R. Lawn and A. G. Evans, “A Model for Crack Initiation in Elastic/Plastic Indentation Fields,” *J. Mater. Sci.*, **12** [11] 2195-2199, (1977).

<sup>17</sup> B. R. Lawn and E. R. Fuller, “Equilibrium Penny-Like Cracks in Indentation Fracture”, *J. Mater. Sci.*, 10 [12] 2016-2024, (1975).

<sup>18</sup> B. R. Lawn, E. R. Fuller, and S. M. Wiederhorn, “Strength Degradation of Brittle Surfaces: Sharp Indentors”, *J. Am. Ceram. Soc.*, **58**, pp. 193-197, (1976).

<sup>19</sup> Wright, A. F., and Leadbetter, A. J. , “The structures of  $\beta$ -cristobalite phases of  $\text{SiO}_2$  and  $\text{AlPO}_4$ ”, *Phil. Mag.* **31**, pp. 1391-1401, (1975).

<sup>20</sup> J.R. Lesniak, STTR Final Report (Contract No. NAS1-97036, 2000). The initial support for its development came from Langley Research Center to Stress Photonics through the STTR Program.

<sup>21</sup> J.R. Lesniak, M.J. Zickel, C.S. Welch, and D.F. Johnson, “An Innovative Polariscope for Photoelastic Stress Analysis”, *Proceedings of the Society of Experimental Mechanics Annual Conference*, Bellevue, WA (June 2-4, 1997), pp. 219-224, (1997).

<sup>22</sup> G. Horn, J. Lesniak, T. Mackin, B. Boyce, *Rev. Sci. Instrum.*, **76**, 045108, pp. 1-10, (2005).

<sup>23</sup> For a more complete discussion see K. Ramesh, “Digital Photoelasticity – Advanced Techniques and Applications”, Berlin, Springer (2000).

<sup>24</sup> There are a number of references on Mohr’s Circle and the application to stresses. For example, one using SI units is Ferdinand P. Beer, E. Russell Johnston, Jr., and John T. DeWolf, “Mechanics of Materials” Third Edition, McGraw-Hill, NY (2001).

<sup>25</sup> While beyond the scope of this work, there are several approaches to build up a structure of short aggregates of dislocations to describe the damage strength. Because fused silica has short-range order and long-range disorder, we use Burgers vectors as a basis for this analysis. One can consider the damage site as a density of edge dislocations, where the extra planes point radially outward (radial symmetry). We assume a collection of edge dislocations with a set of Burgers vectors radially symmetric about the origin, and each of value  $b$ . A reference for dislocations in systems with short-range order (liquids) is given in A. H. Cottrell, “Theory of Dislocations” Gordon and Breach, New York and London, p. 35, (1964).

<sup>26</sup> Lee A Segel, “Mathematics Applied to Continuum Mechanics”, Dover, Mineola, NY, pp. 241-248, (1987).

<sup>27</sup> R. W. Lardner, “Mathematical Theory of Dislocations and Fracture”, University of Toronto Press, Toronto, p. 75 (1974).

<sup>28</sup> R. W. Lardner, pp. 77-78, (1974).

<sup>29</sup> Plastic strain depends upon the path leading to the deformation (i.e. the loading path). We introduce  $\zeta$  as an exponent in the effective length to account for the different paths or classes of impacters, since each shape will have a different dynamic of compression. This is consistent with a power-law expression for the flow curve used in plasticity. See: Dieter, George E, “Mechanical Metallurgy” Third edition, McGraw-Hill, New York, pp.70-72, (1986); and A. Kelly and N. H. Macmillan, “Strong Solids”, 3<sup>rd</sup> Edition, Clarendon Press, Oxford, p.140ff, (1986).

<sup>30</sup> Dieter, George, p. 88, (1986).

<sup>31</sup> After the derivation above, we realize that it is probably not necessary to hold the radius constant, although this point needs to be checked experimentally.

<sup>32</sup> Each chatter check was an elongated damage site created by dragging a stylus across the glass surface. It consisted of a sequence of small indentations in the surface along the stylus path. Consequently the stylus path exceeded the measurement path circumference.

<sup>33</sup> From a process specification for window inspection, Report MT0501-514 “Requirements for Inspection of Orbiter Windows” (Rev G). The Boeing Company, Feb 15, 2008.

<sup>34</sup> This value was found at many internet sites. For example, Proscitech.com, PROPERTIES OF FUSED QUARTZ.

**REPORT DOCUMENTATION PAGE**

*Form Approved  
OMB No. 0704-0188*

The public reporting burden for this collection of information is estimated to average 1 hour per response, including the time for reviewing instructions, searching existing data sources, gathering and maintaining the data needed, and completing and reviewing the collection of information. Send comments regarding this burden estimate or any other aspect of this collection of information, including suggestions for reducing this burden, to Department of Defense, Washington Headquarters Services, Directorate for Information Operations and Reports (0704-0188), 1215 Jefferson Davis Highway, Suite 1204, Arlington, VA 22202-4302. Respondents should be aware that notwithstanding any other provision of law, no person shall be subject to any penalty for failing to comply with a collection of information if it does not display a currently valid OMB control number.  
**PLEASE DO NOT RETURN YOUR FORM TO THE ABOVE ADDRESS.**

<b>1. REPORT DATE (DD-MM-YYYY)</b> 01-12-2011		<b>2. REPORT TYPE</b> Technical Publication		<b>3. DATES COVERED (From - To)</b>	
<b>4. TITLE AND SUBTITLE</b>  Examination of Relationship Between Photonic Signatures and Fracture Strength of Fused Silica Used in Orbiter Windows				<b>5a. CONTRACT NUMBER</b>	
				<b>5b. GRANT NUMBER</b>	
				<b>5c. PROGRAM ELEMENT NUMBER</b>	
				<b>5d. PROJECT NUMBER</b>	
<b>6. AUTHOR(S)</b>  Yost, William T.; Cramer, K. Elliott; Estes, Linda R.; Salem, Jonathan A.; Lankford, James, Jr.; Lesniak, Jon				<b>5e. TASK NUMBER</b>	
				<b>5f. WORK UNIT NUMBER</b>  604746.02.22.07.01.01.04	
				<b>8. PERFORMING ORGANIZATION REPORT NUMBER</b>  L-20101	
<b>7. PERFORMING ORGANIZATION NAME(S) AND ADDRESS(ES)</b> NASA Langley Research Center Hampton, VA 23681-2199				<b>10. SPONSOR/MONITOR'S ACRONYM(S)</b>  NASA	
<b>9. SPONSORING/MONITORING AGENCY NAME(S) AND ADDRESS(ES)</b> National Aeronautics and Space Administration Washington, DC 20546-0001				<b>11. SPONSOR/MONITOR'S REPORT NUMBER(S)</b>  NASA/TP-2011-217322	
<b>12. DISTRIBUTION/AVAILABILITY STATEMENT</b> Unclassified Unlimited Subject Category 37 Availability: NASA CASI (443) 757-5802					
<b>13. SUPPLEMENTARY NOTES</b>					
<b>14. ABSTRACT</b>  A commercially available grey-field polariscope (GFP) instrument for photoelastic examination is used to assess impact damage inflicted upon the outer-most pane of the orbiter windows. Four categories of damage: hyper-velocity impacts that occur during space-flight (HVI); hypervelocity impacts artificially made at the Hypervelocity Impact Technology Facility (HIT-F); impacts made by larger objects falling onto the pane surface to simulate dropped items on the window during service/storage of vehicle (Bruises); and light scratches from dull objects designed to mimic those that might occur by dragging a dull object across the glass surface (Chatter Checks) are examined. The damage sites are cored from fused silica window carcasses, examined with the GFP and other methodologies, and broken using the ASTM Standard C1499-09 to measure the fracture strength. A correlation is made between the fracture strength and damage-site measurements including geometrical measurements and GFP measurements of photoelastic retardation (stress patterns) surrounding the damage sites. An analytical damage model to predict fracture strength from photoelastic retardation measurements is presented and compared with experimental results.					
<b>15. SUBJECT TERMS</b>  Fracture strength; Fused silica; Hypervelocity impact; Impact damage; Photoelastic					
<b>16. SECURITY CLASSIFICATION OF:</b>			<b>17. LIMITATION OF ABSTRACT</b>	<b>18. NUMBER OF PAGES</b>	<b>19a. NAME OF RESPONSIBLE PERSON</b>
<b>a. REPORT</b>	<b>b. ABSTRACT</b>	<b>c. THIS PAGE</b>			STI Help Desk (email: help@sti.nasa.gov)
U	U	U	UU	45	<b>19b. TELEPHONE NUMBER (Include area code)</b>  (443) 757-5802